A&A, 689, A152 (2024)
https://doi.org/10.1051/0004-6361/202348636

Astronomy & Astrophysics

JADES: Carbon enrichment 350 Myr after the Big Bang

Francesco D'Eugenio[1,2,⋆], Roberto Maiolino[1,2,3], Stefano Carniani[4], Jacopo Chevallard[5], Emma Curtis-Lake[6], Joris Witstok[1,2], Stephane Charlot[7], William M. Baker[1,2], Santiago Arribas[8], Kristan Boyett[9,10], Andrew J. Bunker[5], Mirko Curti[11,1,2], Daniel J. Eisenstein[12], Kevin Hainline[13], Zhiyuan Ji[13], Benjamin D. Johnson[12], Nimisha Kumari[14], Tobias J. Looser[1,2], Kimihiko Nakajima[15], Erica Nelson[16], Marcia Rieke[13], Brant Robertson[17], Jan Scholtz[1,2], Renske Smit[18], Fengwu Sun[13], Giacomo Venturi[4], Sandro Tacchella[1,2], Hannah Übler[1,2], Christopher N. A. Willmer[13], and Chris Willott[19]

(Affiliations can be found after the references)

Received 16 November 2023 / Accepted 24 April 2024

ABSTRACT

Finding the emergence of the first metals in the early Universe and identifying their origin are some of the most important goals of modern astrophysics. We present deep JWST/NIRSpec spectroscopy of GS-z12, a galaxy at z = 12.5, in which we report the detection of the C III]λλ1907,1909 nebular emission line. This represents the most distant detection of a metal transition, and the most distant redshift determination based on emission lines. In addition, we report tentative detections of [O II]λλ3726,3729 and [Ne III]λ3869, and possibly O III]λλ1661,1666. By using the accurate redshift obtained from C III], we can model the Lyα drop to reliably measure an absorbing column density of hydrogen of $N_{\rm HI} \approx 10^{22}$ cm^{-2}, which is too high for an IGM origin and implies an abundant neutral ISM in GS-z12 or in the CGM around it. We tentatively infer a lower limit for the neutral gas mass of about $10^7\,M_\odot$ which, compared with the galaxy stellar mass of $\sim 5\times10^7\,M_\odot$, implies a gas fraction higher than about 0.2–0.5. By comparing the measured emission lines with model-based diagnostic diagrams, we derive a solar or even super-solar carbon-to-oxygen ratio, tentatively $\log(\mathrm{C/O}) > -0.21$ dex ($[\mathrm{C/O}] > 0.15$ dex), while a Bayesian modelling of the spectrum indicates $\log(\mathrm{C/O}) = -0.30 \pm 0.07$ dex ($[\mathrm{C/O}] = 0.06 \pm 0.07$ dex). This is higher than the C/O measured in galaxies discovered by JWST at $z = 6$–9, and higher than the C/O arising from Type II supernovae enrichment. Asymptotic giant branch stars can hardly contribute to the observed carbon enrichment at these early epochs and low metallicities. Such a high C/O in a galaxy observed 350 Myr after the Big Bang may thus be explained by the yields of extremely metal-poor stars, and may even be the heritage of the first generation of supernovae from Population III progenitors. A robust determination of the total metallicity in this galaxy is essential to constrain these scenarios.

Key words. stars: Population III – galaxies: abundances – galaxies: formation – galaxies: high-redshift

1. Introduction

The appearance of the first galaxies marks a key phase transition of the Universe (i.e. the end of the dark ages). A keystone of this transition is the start of stellar nucleosynthesis and the diffusion of metals. Extensive theoretical work has been devoted to predicting the properties of the first generation of stars (Population III, hereafter PopIII; e.g. Hirano et al. 2014) and their supernova yields (Heger & Woosley 2010; Limongi & Chieffi 2018). While PopIII stars are thought to be short-lived (with typical masses of 10–40 $M_\odot$; Hosokawa et al. 2011), the chemical signature of their yields may still be observable today. Empirically, extensive searches of PopIII-enriched systems have been undertaken both within the Milky Way (e.g. Frebel & Norris 2015) and in extragalactic absorbers, including in the most metal-poor damped Lyα (DLA) systems (e.g. Pettini et al. 2008; Salvadori & Ferrara 2012; Cooke et al. 2017; Saccardi et al. 2023) and Lyman-limit systems (LLS; Fumagalli et al. 2016; Saccardi et al. 2023).

The launch of JWST enabled, for the first time, the measurement of the physical properties of galaxies out to $z > 10$ (Curtis-Lake et al. 2023; Robertson et al. 2023; Bunker et al. 2023a; Tacchella et al. 2023; Maiolino et al. 2024; Arrabal Haro et al. 2023; Hsiao et al. 2023; Wang et al. 2023). These high-redshift observations challenge the extrapolation of trends of galaxy properties measured at lower redshifts. These trends are generally understood in terms of decreasing gas metallicity (Schaerer et al. 2022; Curti et al. 2024; Nakajima et al. 2023) and increasing density (Reddy et al. 2023), ionisation parameter (Cameron et al. 2023a), temperature (Curti et al. 2023), and stochasticity of their star-formation histories (SFH; Dressler et al. 2024; Endsley et al. 2023; Looser et al. 2023). However, extrapolations of these trends at $z > 10$ do not fully explain the observed properties of galaxies. In particular, observations of galaxies at redshifts $z = 6$–9 suggest that the carbon-to-oxygen abundance ratio $\log(\mathrm{C/O})$[1] decreases with increasing z (Arellano-Córdova et al. 2022; Jones et al. 2023; Stiavelli et al. 2023). At even higher redshift, however, the nebular emission-line ratios in a luminous galaxy at $z = 10.6$ (GN-z11, Oesch et al. 2016; Bunker et al. 2023a) seem to require exotic chemical abundances (Cameron et al. 2023b), proto-globular clusters (Senchyna et al. 2024; Charbonnel et al. 2023), or Wolf–Rayet stars, possibly with a fine-tuned SFH (Kobayashi & Ferrara 2024). Moreover, a supermassive accreting black hole has been identified in this galaxy, suggesting that the peculiar chemical abundances might be primarily associated with its nuclear region (Maiolino et al. 2024).

One reason why the chemical abundance trends identified at lower redshifts may break down at $z > 10$ is that, as our

⋆ Corresponding author; francesco.deugenio@gmail.com

[1] We also express the carbon-to-oxygen abundance in units of the solar abundance, i.e. $[\mathrm{C/O}] \equiv \log(\mathrm{C/O}) - \log(\mathrm{C/O})_\odot$.

observations approach the end of 'Cosmic Dawn' (150–250 Myr after the Big Bang, Robertson 2022), galaxies may carry stronger imprints from the first generation of metal-poor stars, whose physical properties and spectra are poorly understood. In addition to rare objects like the remarkably bright GN-z11, JWST enabled the observations of spectra of regular galaxies at $z = 10-13$ (Curtis-Lake et al. 2023, hereafter CLC23; Hsiao et al. 2023; Arrabal Haro et al. 2023; Wang et al. 2023), at redshifts even higher than GN-z11 (i.e. even nearer to the end of Cosmic Dawn). Being less extreme than objects like GN-z11, these systems are likely to be more representative of the typical physical properties of galaxies at those epochs (CLC23, Robertson et al. 2023). One of the remarkable findings of CLC23 was the lack of any emission line, even with the unprecedented depth of the JWST Advanced Deep Extragalactic Survey (JADES; Eisenstein et al. 2023a; Rieke et al. 2023; Bunker et al. 2023b). Unfortunately, the lack of emission lines severely affects our ability to constrain the physical properties and chemical abundances of these galaxies because systematic model uncertainties dominate the constraints obtained by fitting a line-free spectrum (these uncertainties are introduced through strong priors on the shape of the SFH and on other parameters; CLC23).

To address this shortcoming, the large programme PID 3215 (Eisenstein et al. 2023b), which has obtained deep multi-band imaging, has in parallel also obtained the deepest spectroscopic observations yet of galaxies at $z > 10$. The 50-hour integration with JWST/NIRSpec provides a 5-σ emission-line sensitivity of $10-5\times10^{-20}$ erg s^{-1} cm^{-2} at ≈2–5 μm (for spectrally unresolved lines). In this article, we report the first analysis of the new spectroscopic data for GS-z12, a $z > 10$ galaxy already analysed in CLC23 and Robertson et al. (2023). After presenting the data reduction and analysis in Sect. 2, we show the physical constraints obtained from the data (Sects. 3–5), and conclude with a brief discussion and outlook (Sect. 6).

Throughout this work, we assume the Planck Collaboration VI (2020) cosmology, a Chabrier (2003) initial mass function (IMF) with an upper-mass cutoff of 300 $M_\odot$, and the (initial) solar abundances of Gutkin et al. (2016, i.e. $Z_\odot = 0.01524$ and $\log(C/O) = -0.36$ dex); to convert to the abundances of Asplund et al. (2009), all log (C/O) values should be down-scaled by 0.10 dex. Stellar masses refer to the total stellar mass formed (i.e. the integral of a galaxy SFH), and distances are proper distances.

2. Observations, sample, and data analysis

The observations consist of NIRSpec Micro-Shutter Assembly (MSA) spectroscopy (Jakobsen et al. 2022; Ferruit et al. 2022) with the prism and with the G140M and G395M gratings. These data were obtained as part of programmes PID 1210 (PI N. Lützgendorf; already presented in CLC23 and Bunker et al. 2023b) and PID 3215 (PI D. Eisenstein and R. Maiolino, Eisenstein et al. 2023b). A summary of the observing configurations and total integrations is provided in Table 1. The data reduction was performed exactly as described in Bunker et al. (2023b), Carniani et al. (2024). We used nodding for background subtraction, and extracted the 1-d spectrum using a 3-pixel window. Effective line spread functions (LSF) were obtained from modelling the instrument, as described in de Graaff et al. (2024). The input model for each galaxy was obtained from FORCEPHO (Johnson et al., in prep.), using the same methods as described in Baker et al. (2023). The results are shown in Table 2. We applied a slit-loss correction appropriate for point sources (cf. the morphological parameters reported in Table 2). We note that this slit-loss correction is optimised for a 5-pixel aperture. For the analysis, we combine the data from PIDs 3215 and 1210 using a simple inverse-variance weighting.

Table 1. Summary of the observations from programmes 1210 and 3215.

Disperser	Prism	G140M	G395M
Filter	CLEAR	F070LP	F290LP
Spectral resolution R	30–300	700–1500	700–1500
Exp. time 1210 [h]	18.7	4.7	4.7
Exp. time 3215 [h]	46.7	11.7	46.7 (37.4) [(a)]
Exp. time Total [h]	65.4	16.4	51.5 (42.1) [(a)]

Notes. These exposure times apply only to GS-z12; other targets in the two programmes may have different exposure times, depending on the mask allocation. [(a)]The last visit was affected by short circuits in the MSA (Rawle et al. 2022), and the true exposure time in PID 3215 is reduced to 37.4 h.

Table 2. Morphological parameters of GS-z12.

R_e	[arcsec]	0.040 ± 0.003
PA	[degree]	70 ± 6
Axis ratio q	–	0.55 ± 0.07
Sérsic index	–	0.90 ± 0.09

Notes. FORCEPHO photometry was obtained as explained in Baker et al. (2023).

In the left column of Fig. 1 we display NIRCam imaging for GS-z12 (panel a), with overlaid the configuration of the NIRSpec MSA shutters in PID 3215 (these observations consist of five dithered pointings). The 2-d signal-to-noise ratio (S/N) and the boxcar extracted 1-d spectrum are shown in panels b and c.

Panel a shows a contaminant with low surface brightness to the west (marked by an asterisk). This contaminant also appears at the top of the 2-d S/N map (panel 1b), and its presence was taken into account in the data reduction. Nevertheless, for the prism data of 3215, we measured a negative flux blueward of the Lyα drop. The origin of this artefact is still unclear. To remove it, we extracted two background spectra from the 2-d spectrum (above and below the object trace), fitted a declining exponential function to these data, and removed the average best-fit background model from the 1-d spectrum. This procedure has no detectable impact on the emission-line fluxes, but affects the shape of the continuum and Lyα drop. The uncertainties from the data reduction pipeline were validated by inspecting the dispersion of the individual integrations in each wavelength channel (Appendix A). Overall, we find that the data-reduction pipeline gives more conservative noise estimates than bootstrapping, which is expected because bootstrapping does not take into account correlated noise, while the data reduction pipeline uses variance-conserving resampling to capture the loss of information due to correlated noise (Dorner 2012).

2.1. Emission-line fitting

Emission-line fluxes and equivalent widths (EW) were measured using a local pixel-integrated Gaussian model with linear background, in a window of 0.3 μm on either side of the expected line location. The lines were assumed to be spectrally unresolved (Gaussian σ equal to one spectral pixel). The model has four free parameters: flux, redshift, and two coefficients for the background. The redshift was constrained to be centred at $z = 12.479$ using a Gaussian prior with dispersion set to 0.014 (this red-

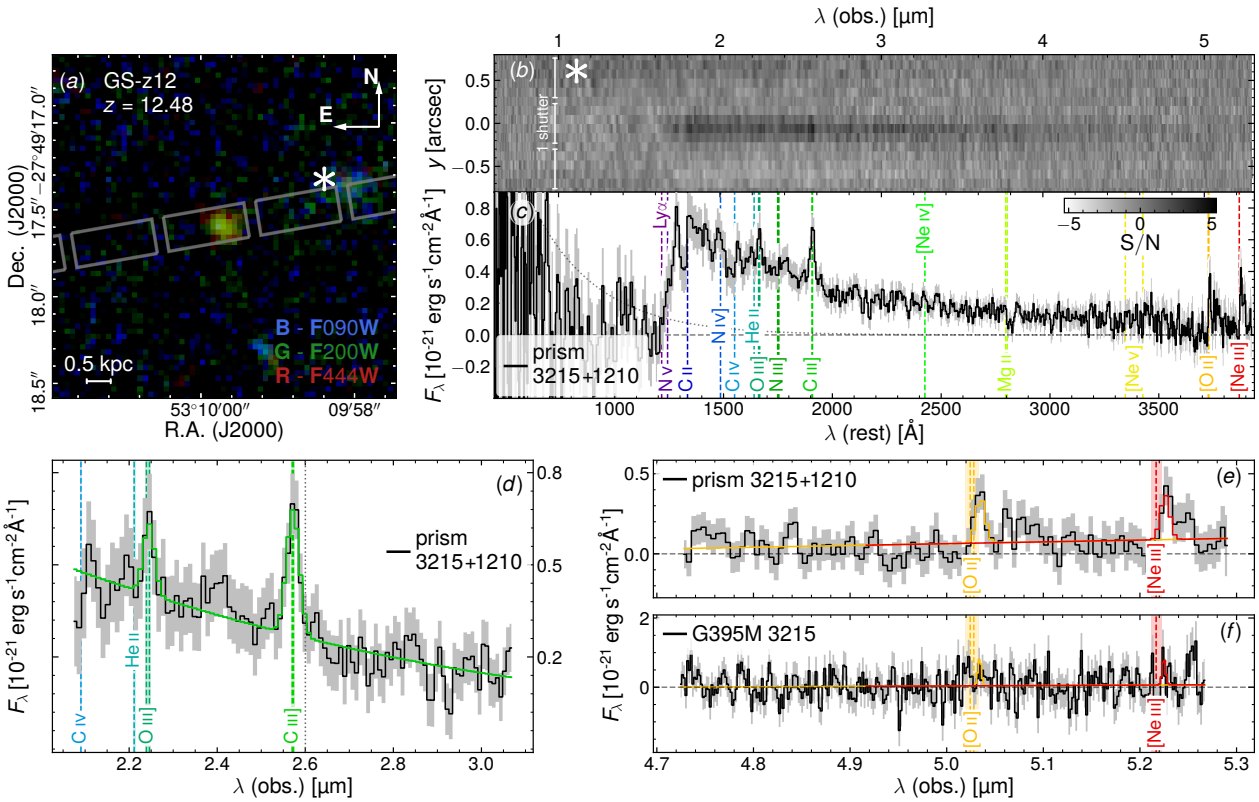

Fig. 1. Summary of our observations. Panel a; false-colour RGB image, highlighting the position of the NIRSpec/MSA shutters in PID 3215. The asterisk indicates the position of an interloper with low surface brightness, which was removed in the data reduction. Panel b; 2-d S/N map, showing the three central shutters (the asterisk is the position of the interloper). Panel c; 1-d boxcar-extracted prism spectrum, combining 3215 and 1210; the vertical dashed lines marking the position of strong emission lines at $z = 12.48$. Panels d–f; combined 3215 and 1210 data and model spectrum around the O III], C III], [O II] and [Ne III] lines, for the prism (panels d and e) and for the G395M grating (only 3215; panel f). C III] is detected at the 5-σ level (7-σ with the bootstrapping method). O III] is not robustly detected (2.3-σ significance); [O II] and [Ne III] are marginally detected only in the prism (4- and 3.5-σ) but not in the grating, despite comparable sensitivity. The vertical dashed lines mark the wavelength of the emission lines at the redshift of the object, with the shaded region indicating the redshift uncertainty.

shift dispersion is the uncertainty we derived from the redshift estimate, see Sect. 2.2). The fiducial values and uncertainties were estimated using a Markov chain Monte Carlo integrator (Foreman-Mackey et al. 2013); the results are reported in Table 3.

The emission lines O III]λλ1661,1666, C III]λλ1907,1909, [O II]λλ3726,3729, and [Ne III]λ3869 (hereafter simply O III], C III], [O II], and [Ne III]) are central to our analysis of chemical abundances and for this reason are measured adopting a different strategy compared to all the other lines. In addition, while O III] and C III] are observed only by the prism, [O II] and [Ne III] are covered both by the prism and by the G395M grating. Therefore, to take full advantage of the 100-h total integration for [O II] and [Ne III], we fit simultaneously the prism and grating spectra. The model uses six pixel-integrated Gaussians, one each for O III] and C III] (only present in the prism spectrum), and two each for [O II] and [Ne III] (which require separate models for the prism and grating spectra). In total, the model has sixteen free parameters. C III] has three free parameters (flux, width, and redshift for the prism only); O III] has two free parameters, flux and redshift for the prism only; its width is constrained to be the same as C III], and its redshift has a Gaussian prior centred on the C III] redshift and with $\sigma_z = 0.02$. [O II] and [Ne III] are treated as unresolved, hence have a fixed Gaussian dispersion equal to one spectral pixel (as appropriate for the prism and grating separately). The redshifts of [O II] are free and independent in the prism and grating, but we apply Gaussian priors of width $\sigma_z = 0.02$ to maintain them consistent with C III]. This gives two free parameters (with strong priors). The redshifts of [Ne III] are the same as for [O II] in each of the two disperser configurations. For both [O II] and [Ne III], the prism flux is a free parameter, while the grating flux is set to the prism flux up-scaled by 11% (to take into account the systematic flux calibration discrepancy between these two observing modes, e.g. Bunker et al. 2023a). In total, we have nine free parameters describing six Gaussian line shapes. We further add seven parameters to model the local background. The background around C III] and O III] in the prism is modelled with a second-order polynomial (three free parameters); the background around [O II] and [Ne III] is modelled with a straight line, requiring two parameters each for the prism and for the grating spectrum. The prism spectral resolution and detector sampling prevent us from resolving the two variable-ratio doublets C III] and [O II]. We therefore adopt wavelengths of 1907.71 and 3728.49 Å, respectively, obtained by averaging the vacuum wavelengths of the two lines in each doublet. Depending on the doublet ratio for C III] and [O II], this choice introduces a systematic error of up to 0.1 and 0.4 pixels.

A summary of the emission lines and of their fluxes (or upper limits) is provided in Table 3.

2.2. Detection of C III]

We adopt a detection threshold of 5 σ, and report the detection of an emission line at 2.57 μm, with a 5-σ significance. This S/N estimate is based on the conservative uncertainties reported by

Table 3. Nebular emission lines for GS-z12.

	Line(s)	Flux	EW
PRISM	N IV]λ1486	<3.3	<6.4
	C IVλλ1549,1551	<3.3	<5.5
	He IIλ1640	<2.6	<4.2
	O III]λλ1661,1666 [(a)]	(6.0 ± 2.6)	8 ± 3
	N III]λλ1747–1754	<2.2	<3.8
	C III]λλ1907,1909 [(a)]	**12.4 ± 2.5**	**30 ± 7**
	[Ne IV]λλ2422,2424	<1.0	<3.9
	Mg IIλλ2796,2803	<0.8	<4.6
	[Ne V]λ3426	<1.0	<8.6
	[O II]λλ3726,3729 [(a)]	(3.5 ± 0.8)	41 ± 12
	[Ne III]λ3869 [(a)]	(3.3 ± 0.9)	39 ± 13
G140M	Lyα	<5.8	–
	N Vλλ1239,1243	<6.1	–
G395M	[Ne IV]λλ2422,2424	<1.2	–
	Mg IIλλ2796,2803	<1.3	–
	[Ne V]λ3426	<2.9	–
	[O II]λλ3726,3729	<1.7	–
	[Ne III]λ3869	<2.7	–

Notes. Spectral measurements from the three dispersers. Fluxes are in units of 10^{-20} erg s^{-1} cm^{-2}, EWs are in (rest-frame) Å. All uncertainties and upper limits are one standard deviation. Empty entries in the EW column are due to weak or non-detected continuum. The only secure detection, C III], is highlighted in bold. Fluxes in round parentheses (O III], [O II] and [Ne III]) are considered not detected (Sect. 2.3). All uncertainties use the conservative uncertainties from the data reduction pipeline (a discussion of alternative estimates of the uncertainties is given in Appendix A). [(a)]Lines modelled simultaneously across the prism and G395M grating. All other lines are modelled as an unresolved Gaussian, centred around the redshift of C III].

the data reduction pipeline (bootstrapping the data to estimate the uncertainties would increase the significance to 7 σ, as discussed in Appendix A). At the redshift initially estimated by CLC23 from the Lyα drop ($z = 12.6 \pm 0.05$), the line emission at 2.57 μm is significantly offset (2600 km s^{-1}, i.e. one spectral resolution element) from the expected location of C III] (the closest emission line; the expected location is highlighted by the vertical dotted line in Fig. 1d). However, in addition to the formal significance, other pieces of evidence contribute to confirming that this is a solid detection. The comparison of the two independent datasets 3215 and 1210 (Fig. A.1g) shows that the line is seen independently, at the expected level of significance, in both observations. The robustness of the line detection is also confirmed by the visual inspection of the 2-d spectrum, in which the line is observed on three pixels in the spatial direction along the slit. Based on these various lines of evidence, we interpret this line as C III], making it the most distant metal line detection to date.

We measure a high EW(C III]) = 30 ± 7 Å. Similarly high EW(C III]) have been found in some local metal-poor dwarf galaxies, such as Pox 186 ($M_\star \approx 10^5$ M$_\odot$; Kunth et al. 1981; Kumari et al. 2024), considered a local analogue of high-redshift star-forming galaxies, as well as in more massive galaxies at intermediate redshifts ($2 < z < 4$; Le Fèvre et al. 2019) and at $7 < z < 9$ (Stark et al. 2017).

With our joint modelling fit, i.e. including the tentative detections of other lines discussed in the next section, we find a redshift of $z = 12.482 \pm 0.012$. Modelling only C III] at the mean rest-frame wavelength of 1907.71 Å, we find $z = 12.479 \pm 0.014$. In both cases, there is a clear shift with respect to the earlier redshift measurement based off the observed wavelength of the Lyα drop (CLC23). We interpret this redshift discrepancy as evidence for a high column density of cold gas in the inter-stellar medium (ISM) of GS-z12, or in its immediate surroundings, whose Lyα damping wings affect the Lyα drop; this will be further discussed in Sect. 4.

2.3. Additional tentative detections and upper limits

In Table 3 we also report a tentative detection of O III] (2.3-σ significance, or 3.5-σ if adopting the bootstrap method discussed in the Appendix). This line is found at a wavelength consistent with the redshift of C III], but it is not detected in the 1210 and 3215 observations taken separately (Fig. A.1).

Similarly, there appears to be a C IVλλ1549,1551 (hereafter C IV) P-Cygni line at rest-frame 1550 Å, and a blue-shifted absorption of C IIλ1334. If confirmed, these might trace a galactic outflow, but the high implied velocities of about 3000 km s^{-1} would require an AGN. On the basis of current data, these features are considered undetected.

Table 3 also reports tentative detections of [O II] (at 4.4 σ) and [Ne III] (at 3.7 σ). Both lines are below the adopted threshold of 5 σ. In addition to this threshold criterion, we do not consider these lines to be secure detections for the reasons discussed in detail in Appendix A. The arguments in favour of a detection are the correct inter-line wavelength separation, and the combined S/N from the two lines. Yet, several arguments cast doubts about their detection: (i) the moderate (2-σ) tension between the redshifts of C III] and [O II]–[Ne III] (the dashed vertical lines and shaded region in Fig. 1f show the expected location of these lines given the C III] redshift and its associated uncertainty). (ii) the unphysical wavelength offset of 2 pixels of [O II] measured in 1210 with respect to 3215 (cf. cyan and sand lines in Fig. A.1h). (iii) while [Ne III] appears in both datasets at the same wavelength, its profile in 1210 appears to be too narrow and is consistent with a noise spike. (iv) visually inspecting the 2-d S/N map (Fig. 1b), we find no strong evidence for either [O II] or [Ne III] (unlike for C III], which is clearly visible); [O II], in particular, appears to originate from a single spaxel, which would be unphysical, because at 5 μm the JWST point spread function is well sampled by the NIRSpec pixels, so we would expect the line to be spatially extended (like C III]). A more detailed analysis of the NIRSpec/MSA noise characteristics will be presented in P. Jakobsen (in prep.).

The above difficulties with the 4- and 3-σ tentative detections justify our choice of a 5-σ detection threshold. Based on this value, we only consider the C III] detection as solid. We adopt 3-σ upper limits (99.9% confidence) on C IV, [O II] and [Ne III]. Nevertheless, promoting [O II] and [Ne III] to detections would not alter our conclusions. To help the reader judge the effect of assuming both [O II] and [Ne III] to be detected, where relevant we report the results when assuming detections, marking them with a small † symbol (Sect. 5).

3. Spectral modelling with BEAGLE

We fit, pixel-by-pixel, the prism spectrum using the Bayesian modelling tool BEAGLE (Chevallard & Charlot 2016). We mask the region around Lyα because our modelling does not properly account for the (resonant) radiative transfer of Lyα photons. We assume an upper-mass cutoff of the IMF of 300 M$_\odot$ and a star-formation history (SFH) described by a delayed exponential function plus a burst of 10 Myr duration, during which the SFR is assumed to be constant. The adopted SFH decouples the present SFR, which determines the strength of the (line and continuum)

Table 4. Adjustable parameters and associated priors used in the BEAGLE analysis.

Parameter	Symbol	Prior
Redshift	z	$\mathcal{N}(12.48, 0.05)$
Stellar mass formed (integral of the SFH)	$\log(M_\star/\mathrm{M}_\odot)$	$\mathcal{U} \in [6, 12]$
Metallicity of stars with $t > 10$ Myr	$\log(Z_\star/Z_\odot)$	$\mathcal{U} \in [-2.2, 0.4]$
Age of the oldest stars	$\log(t/\mathrm{yr})$	$\mathcal{U} \in [6, 10.8\,^{(a)}]$
Timescale of the delayed exponential SFH	$\log(\tau/\mathrm{yr})$	$\mathcal{U} \in [6, 12]$
SFR during the last 10 Myr of the SFH	$\log(\mathrm{SFR}/\mathrm{M}_\odot\mathrm{yr}^{-1})$	$\mathcal{U} \in [-4, 4]$
V-band attenuation optical depth	$\hat{\tau}_V$	$\exp(-\hat{\tau}_V) \in [0, 6]$
Ionisation parameter	$\log(\mathrm{U})$	$\mathcal{U} \in [-4, -1]$
Dust-to-metal mass ratio	ξ_d	$\mathcal{U} \in [0.1, 0.5]$
ISM metallicity	$\log(Z_{ISM}/Z_\odot)$	$\mathcal{U} \in [-2.2, 0.4]$
Carbon-to-Oxygen abundance	[C/O]	$\mathcal{U} \in [-1, 0.15]$

Notes. $\mathcal{N}(a, b)$ indicates a Normal distribution with mean a and standard deviation b; $\mathcal{U} \in [a, b]$ indicates a Uniform distribution between a and b. $^{(a)}$In practice, BEAGLE will not allow the age of the oldest stars to be greater than the time elapsed between $z_{max} = 30$ and the sampled redshift.

Table 5. Constrains on the physical properties of GS-z12 obtained with BEAGLE using the approach described in Sect. 3.

Parameter	Units	Value
$\log M_\star$	[dex $\mathrm{M}_\odot$]	7.68 ± 0.19
$\log \mathrm{SFR}$	[dex $\mathrm{M}_\odot\,\mathrm{yr}^{-1}$]	0.21 ± 0.07
$\hat{\tau}_V$	–	0.20 ± 0.07
$\log(\mathrm{U})$	[dex]	-1.96 ± 0.25
ξ_d	–	0.24 ± 0.1
$12 + \log(\mathrm{O/H})$	[dex]	7.59 ± 0.25
[C/O]	[dex]	0.06 ± 0.07
$\log(\mathrm{C/O})$	[dex]	-0.30 ± 0.07

nebular emission, from the past one, which mainly contributes to the galaxy stellar mass $M_\star$. We adopt a single metallicity to describe the interstellar metallicity Z_{ISM} and the metallicity of stars younger than 10 Myr (which power the nebular emission), while we let the metallicity of stars older than 10 Myr $Z_\star$ free to vary. The gas-phase metallicity is linked to the interstellar one via the dust-to-metal mass ratio ξ_d, which we vary between 0.1 and 0.5, and which accounts for the differential depletion of heavy elements onto dust grains. To account for dust attenuation, we employ the Charlot & Fall (2000) prescription and fix the fractional attenuation due to the diffuse ISM to 0.4. We also account, for the first time, for a varying carbon-to-oxygen abundance C/O in the range 0.1–1.4 the solar abundance, adopting the grid of photoionisation models of Gutkin et al. (2016, hereafter: G16). We report the priors adopted for the different adjustable parameters of the model in Table 4.

We show in Table 5 the physical properties of GS-z12 derived from BEAGLE. Fig. 2 shows the posterior probability distribution obtained from BEAGLE; for conciseness, we only report the model parameters most relevant to our science analysis. We find that the observed spectrum is best reproduced by models with $[\mathrm{C/O}] = 0.06$ dex (1.15× the solar C/O abundance; corresponding to $\log(\mathrm{C/O}) = -0.30 \pm 0.06$ dex). This is a key result that we discuss in Sect. 5. In this section, we focus on the remaining physical properties. In addition to C/O, we obtain constraints on $M_\star = 7.68 \pm 0.19\,\mathrm{M}_\odot$, $\log \mathrm{SFR} = 0.21 \pm 0.07\,\mathrm{M}_\odot\,\mathrm{yr}^{-1}$, and $\hat{\tau}_V = 0.20 \pm 0.07$. The fit indicates a gas-phase oxygen abundance of $12 + \log(\mathrm{O/H}) = 7.59 \pm 0.25$. This value is primarily constrained by the (presence and absence) of emission lines.

From the BEAGLE-derived $M_\star$, assuming virial equilibrium and the empirical relation of Cappellari et al. (2013), we infer a second moment of the velocity distribution $\sigma \approx 20\,\mathrm{km\,s}^{-1}$, validating our choice of assuming all emission lines to be spectrally unresolved. Clearly, this is only an order-of-magnitude calculation, because the assumed virial relation is calibrated from early-type galaxies in the local Universe (Cappellari et al. 2013). In particular, our estimate does not take into account gas and dark matter; however, even assuming a total mass ten times larger than $M_\star$, we would obtain $\sigma \approx 65\,\mathrm{km\,s}^{-1}$, still below the spectral resolution of our data.

We note that the point-source corrections are optimised for a 5-pixel extraction box, but we use the 3-pixel extraction to maximise the S/N. Nevertheless, we tested that, when modelling either the 3-pixel or 5-pixel extracted spectra, BEAGLE recovers statistically consistent values of $M_\star$, SFR and $12 + \log(\mathrm{O/H})$. The dust attenuation is, however, inferred to be approximately 2× higher when fitting to a 5-pixel extracted spectrum, suggesting that the slope is somewhat more blue in this 3-pixel extraction (as expected, because more flux is lost at longer wavelengths).

4. A large reservoir of cold and metal-poor gas

By fixing the redshift to $z = 12.48$, we can also study the Lyα absorption profile in more detail. The clear shift between the rest-frame wavelength of Lyα and the Lyα drop implies a very strong damping-wing absorption, well beyond what is expected from the neutral intergalactic medium (IGM) at such high redshifts (e.g. Heintz et al. 2024). The observed profile can be well explained in terms of Lyα absorption in the ISM of the galaxy, or in its surrounding (cold) circumgalactic medium (CGM), similarly to what is observed in DLA systems (Fig. 3). To study the neutral hydrogen absorption in more detail, we consider the maximum-a-posteriori BEAGLE spectrum, where we have fitted the prism spectrum while masking the region around Lyα. We then used this fiducial intrinsic spectrum in the Bayesian inference method described below.

To model the combined effect of the DLA and IGM, we used the publicly available software `lymana_absorption`. First, we attenuated the BEAGLE spectrum with the absorption profile of a DLA system parametrised only by the column density of neutral hydrogen, N_{HI}[2]. Second, we applied an additional absorption profile arising from neutral gas in the intervening IGM. This is characterised by a (global) neutral hydrogen fraction $\bar{x}_{HI}$

[2] We assumed that the DLA system is centred on the systemic redshift of the galaxy, as the spectral resolution at the observed wavelength of Lyα ($\sim$4000 km s^{-1}) does not allow us to constrain the infall velocities of gas in the CGM For the same reason, we note that a pure IGM absorption profile (Fig. 3) would require an unphysically large infall velocity to resolve the significant discrepancy with the observed spectrum.

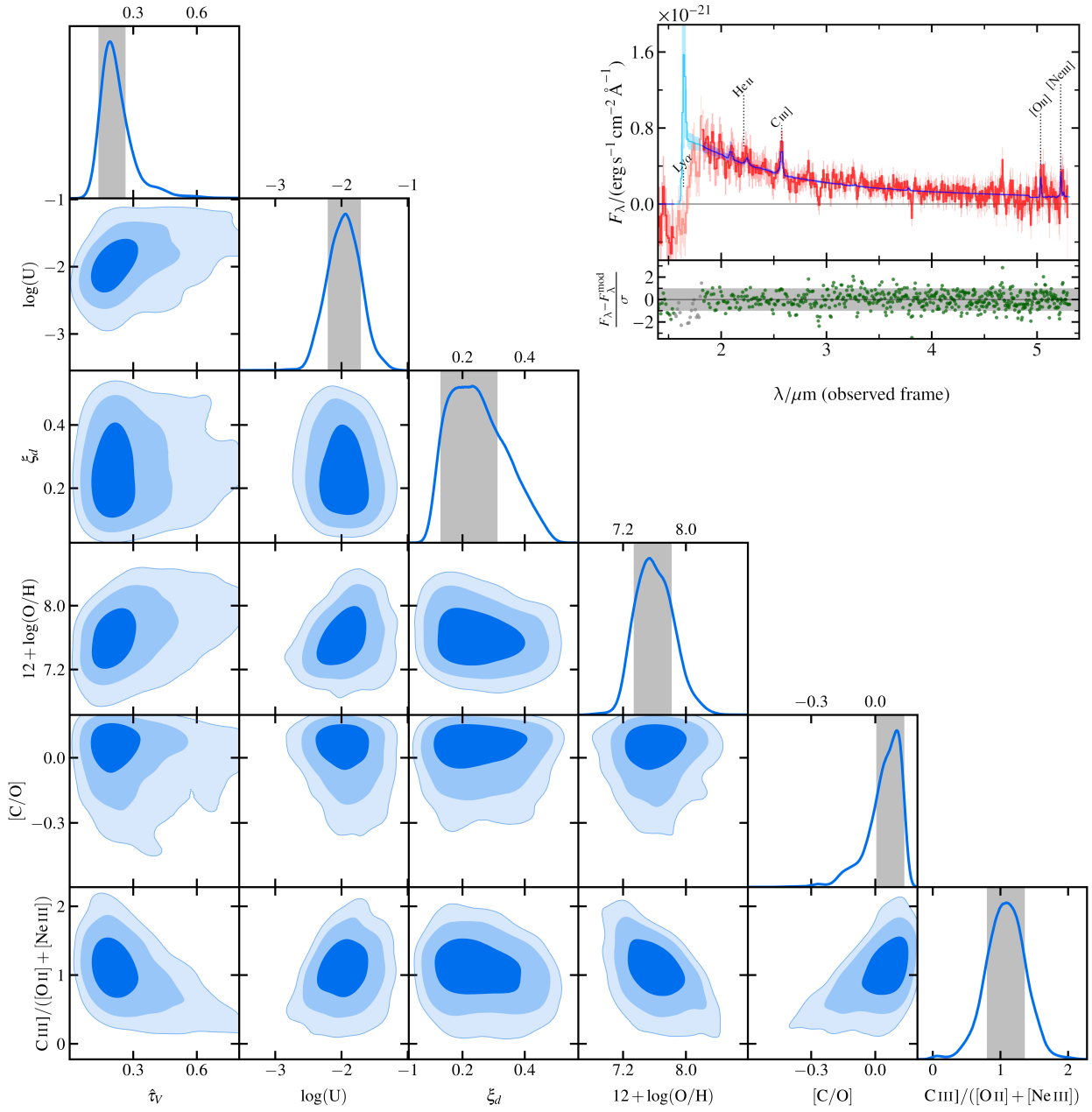

Fig. 2. Posterior probability distribution obtained from BEAGLE, illustrating the subset of model parameters most relevant to this work. From left to right, the effective V-band dust attenuation optical depth $\hat{\tau}_V$, ionisation parameter log (U), dust-to-metal mass ratio ξ_d, gas-phase metallicity $12 + \log(\mathrm{O/H})$, C/O abundance (in logarithmic units of the solar C/O abundance), and predicted line ratio C III]/([O II]+[Ne III]), which is the main empirical constraint coming from the NIRSpec spectrum. The analysis with BEAGLE suggests that our data are best reproduced by models with slightly super solar C/O abundance. The inset diagram shows the NIRSpec data (red) and their uncertainties (light red), as well as the model predictions from BEAGLE (in blue the posterior median, while the shaded light blue region indicates the 68% credible region). The bottom panel shows the residual in units of σ, the observational error, with the grey band encompassing $\pm 1\,\sigma$. We mask the region around Lyα, since we do not model this line self-consistently.

(under the standard assumption that the gas has mean cosmic density and $T = 1$ K; for more details, see Witstok et al. 2024). The temperature of the IGM does not impact our results, nor does the temperature of the DLA (we used 100 K as default, but also tested 1 K and 10 000 K finding no difference in the absorption profile). We computed the likelihood based on the inverse-variance weighted squared residuals between a given model convolved by the effective LSF (Sect. 2) and the observed prism spectrum. The logarithm of neutral hydrogen column density, $\log N_{\mathrm{HI}}/(\mathrm{cm}^2)$, is allowed to vary under a uniform prior distribution between values of 20 and 23, while the neutral hydrogen fraction of the IGM is fixed to $\bar{x}_{\mathrm{HI}} = 1$. This is our fiducial model, which finds a neutral hydrogen column density $\log N_{\mathrm{HI}}/(\mathrm{cm}^2) = 22.3 \pm 0.1$. Alternatively, leaving $\bar{x}_{\mathrm{HI}}$ free to vary with a uniform prior $0 \leq \bar{x}_{\mathrm{HI}} \leq 1$, we estimated a neutral hydrogen column density $\log N_{\mathrm{HI}}/(\mathrm{cm}^2) = 22.1^{+0.2}_{-0.3}$, statistically consistent with the fiducial model. Both cases clearly require the presence of dense neutral gas in or around GS-z12, as opposed to only the diffuse IGM. In the following, we use the first estimate as our fiducial value, because the data is unable to fully constrain $\bar{x}_{\mathrm{HI}}$.

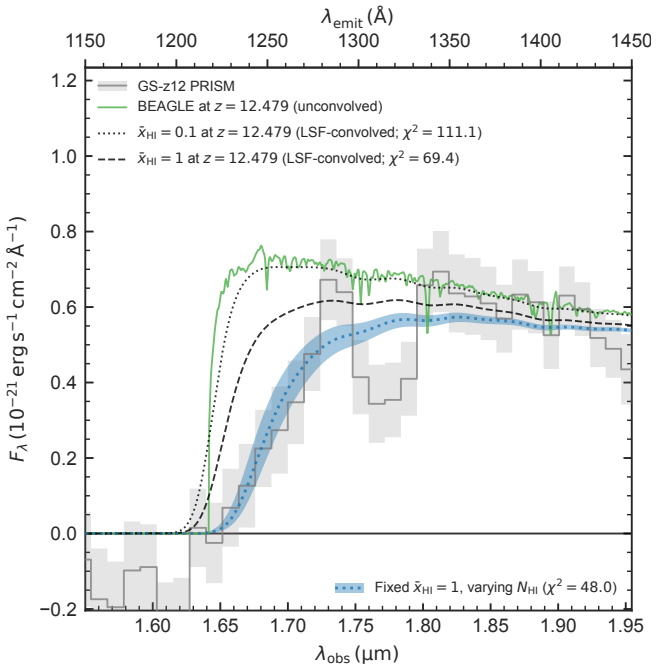

Fig. 3. Fiducial (maximum-a-posteriori) BEAGLE spectrum (green) and data (grey) around the Lyα transition. The dashed black line shows the effect of convolving the model spectrum with the prism LSF. The best-fit absorption profiles combining IGM and DLA absorption are shown by the dotted blue line and blue shading, assuming a fixed IGM neutral hydrogen fraction $\bar{x}_{HI} = 1$. We tested a model with varying $\bar{x}_{HI}$, but this parameter is not well constrained, mainly because significant additional absorption is required to reconcile the profiles with the observed spectral break even with maximum IGM absorption ($\bar{x}_{HI} = 1$; see text for details).

Assuming that the dust attenuation through this neutral medium is the same as through the diffuse ISM of GS-z12, i.e. $\tau_V = 0.08 \pm 0.03$ (obtained as $0.4 \cdot \hat{\tau}_V$, see Sect. 3), we can derive an order-of-magnitude estimate of the metallicity of the DLA gas as

$$Z_{DLA} = Z_{MW} \frac{(\tau_V / N_{HI})_{DLA}}{(\tau_V / N_{HI})_{MW}} \cdot \frac{\xi_{d,MW}}{\xi_{d,DLA}}. \quad (1)$$

The gas-to-extinction ratio we observe in the Milky Way is $N_{HI}/\tau_V = (1.92 \pm 0.02) \times 10^{21}$ cm^{-2} (e.g. Zhu et al. 2017); the dust-to-metal ratio is $\xi_{d,MW} = 0.45$ (e.g. Konstantopoulou et al. 2024). The metallicity of the ISM in the solar neighbourhood is 0.2 dex lower than solar (Arellano-Córdova et al. 2021), therefore, we assume $Z_{MW} = 0.6$ solar.

At low metallicity and at high gas fractions (as appropriate for GS-z12) ξ_d is lower (De Cia et al. 2016; De Vis et al. 2019). Assuming a metallicity in the range 0.03–0.1 solar, the typical ξ_d measured in high-redshift absorbers is 0.24 ± 0.11[3] (e.g. Konstantopoulou et al. 2022). These values are on average half the Milky Way value. The above formula then gives us a DLA metallicity of $Z_{DLA} = 0.005$–$0.02\,Z_\odot$ ($12 + \log(O/H) = 6.6$–7.2 dex), lower than the estimate from Sect. 3. We note that the large uncertainties in our assumptions are compounded by systematics in the spectral modelling with BEAGLE. For instance, using a 5-pixel extraction window (instead of the default 3-pixel) increases τ_V by approximately a factor 2. In addition, the optical depth τ_V estimated with BEAGLE relies on an attenuation law (including absorption and scattering into and out of the line of sight caused by local and global geometric effects), while the column density from the DLA-like fit assumes a pure foreground extinction curve (including absorption and scattering only out of the line of sight). Adopting an extinction rather than an attenuation curve in BEAGLE would provide lower τ_V, which would lower the metallicity estimate. Therefore, in the following, we treat our mean metallicity estimate for the DLA of 6.9 dex as an upper limit.

Assuming all this gas is from the galaxy's ISM and that the DLA comes mostly from within one R_e, we can estimate the mass of atomic gas as $M_{gas} = 2\,(1.34\,m_H\,N_{HI})\,\pi q R_e^2$, giving $\log(M_{gas}/M_\odot) = 7.1 \pm 0.2$ (where m_H is the mass of the hydrogen atom, the factor 1.34 accounts for the helium fraction, the additional factor of two is a geometric factor assuming equal column density on the far side of the galaxy, and q is the axis ratio of the galaxy; we used the morphological parameters from Table 2). This gas mass is 20–50% of the stellar mass inferred by BEAGLE. However, this is only the mass of atomic hydrogen and does not take into account the fraction of molecular (or ionised) hydrogen, hence it should be considered a lower limit. Such a gas fraction (or even higher given that it is a lower boundary) is consistent with many other galaxies at high redshift (Tacconi et al. 2020). Indeed, assuming that the neutral gas extends out to $3\,R_e$ (as suggested by observations of [C II]λ158 μm at lower redshifts; Fudamoto et al. 2022), we would obtain a gas mass that is nine times larger, and a gas-to-stellar mass fraction more in line with numerical simulations (Heintz et al. 2024).

The corresponding lower limit on the gas surface density is $150\,M_\odot\,pc^{-2}$, at the boundary between normal star-forming regions and starbursts galaxies in the local Universe (e.g. Kennicutt & Evans 2012). At these densities, most cold gas in the local Universe is expected to be in the molecular phase.

The SFR density inferred combining BEAGLE and the size measurement is of order $25\,M_\odot\,yr^{-1}\,kpc^{-2}$. Together with the gas surface density estimated above, this value places GS-z12 above the Schmidt–Kennicutt (S–K) relation, near local starburst galaxies. However, it could be consistent with the S–K relation considering that the surface density inferred above is a lower limit, and implying, once again, that a significant fraction of the gas is in molecular form.

5. Source of photoionisation and chemical abundances

To identify the source of photoionisation in GS-z12, we rely on models from the literature. The high value of EW(C III]) rules out pristine sources like Population III stars and direct-collapse black holes (Nakajima & Maiolino 2022; hereafter NM22). We therefore focus on star-formation and AGN photoionisation, using models from NM22, Feltre et al. (2016, hereafter F16), and Gutkin et al. (2016, hereafter G16). In the following, the grids of star-forming models are marked with stars, and those of AGNs are marked by triangles. For the star-forming models of NM22, we fix the upper-mass cutoff of the IMF to $300\,M_\odot$; for their AGN models, we fix the shape of the ionising continuum to have a slope $\alpha_{AGN} = -2$. In both cases, the density is $n_e = 10^3$ cm^{-3}. For the star-forming models of G16, we fix the upper-mass cutoff of the IMF to $300\,M_\odot$, the dust-to-metal mass ratio $\xi_d = 0.1$, the maximum stellar age to 100 Myr, and the density to $n_e = 10^2$ cm^{-3}. For the AGN models of F16, we fix both $\xi_d = 0.1$ and $n_e = 10^3$ cm^{-3}. We colour-code the external enve-

[3] We took the median of DLAs illuminated by GRBs, but taking the median of DLAs illuminated by QSOs would change the ξ_d by a factor of ≈2, which is still within the large scatter of these measurements.

lope of some of the grids by their metallicity Z and ionisation parameter log (U). Each of these models presents unique advantages: NM22 extend to very low metallicity, and also provide EWs; the other two models provide independently varying C/O abundances.

In Figs. 4a–b the green hexagon shows the NIRSpec 3-σ upper limits in the UV diagnostic diagram using C IV, C III] and He IIλ1640 (hereafter He II; F16; G16). We also report the position of the local analogue Pox 186 as a cross; while the stringent upper limits on Pox 186 place it confidently in the star-forming region of the diagram, GS-z12 is in the upper envelope of the AGN models (panel a). Given the trend of increasing C III]/He II with decreasing metallicity, we expect that extending the metallicity range of the F16 grid to lower values would also allow these models to overlap with GS-z12. In Fig. 4c, we show EW(C III]) vs. C IV/C III] for the NM22 models; both GS-z12 and the local analogue Pox 186 cannot be explained by either star-formation or AGN photoionisation. However, we note that the NM22 models assume the C/O enrichment scaling derived from the local Universe (Dopita et al. 2006); therefore, at the lowest metallicities relevant to this work, their C/O abundance is significantly sub-solar, and actually closer to the pure yield of Type II supernovae.

In Fig. 5 we explore the C/O abundance ratio using the line ratio C III]/([O II]+[Ne III]), leveraging the fact that both O and Ne are α elements released by Type II supernovae. Assuming that neither [O II] nor [Ne III] is detected, the resulting 3-σ lower limit on C III]/([O II]+[Ne III]) = 3.4 cannot be explained by the standard enrichment pattern at the root of the models of NM22 (panel a). In contrast, the star-forming models of G16 allow C/O to vary independently of the total metallicity. To explain the observations of GS-z12 (green hexagon), these models require a super-solar [C/O] $\approx$ 0.15 dex (i.e. near the highest value explored by the G16 models and corresponding to log (C/O) = −0.21 dex). This is in agreement with the results from BEAGLE (Sect. 3), which find [C/O] = 0.06 ± 0.07. Even assuming [O II] and [Ne III] detections, we would measure a line ratio of 1.8±0.5, yielding a [C/O] $\approx$ 0 dex (grey hexagon, log (C/O) = −0.36). This abundance pattern, with solar or higher-than-solar C/O, would also alleviate the tension with the EW measurements (Fig. 4c). Changing the upper-mass cut of the IMF from 300 to 100 $M_\odot$ and the maximum stellar age from 100 to 10 Myr does not change our conclusions. Increasing the dust-to-metal mass fraction ξ_d from 0.1 to 0.3 would instead make our conclusions even stronger, by lowering the predicted C III]/([O II]+[Ne III]) ratio (because C has a higher depletion than Ne and O). We note that the BEAGLE-based analysis provides only mild constraints on $\xi_d = 0.24 \pm 0.1$.

In addition to these diagnostic diagrams, the Bayesian approach of BEAGLE enables to simultaneously take into account all the data and the degeneracies between the various model parameters. BEAGLE predicts a C/O value of [C/O] = 0.06 ± 0.07 which, as we mentioned, is very near to the highest value explored by the photoionisation model grid of G16. The BEAGLE modelling predicts a C III]/([O II]+[Ne III]) ratio in the range 0.79−1.36 (68% credible region) – lower than our empirical upper limit of 3.4, but consistent with the value of 1.8 ± 0.5 we find assuming both [O II] and [Ne III] to be detected.

In principle, we could also use O III] to estimate [C/O], but this is complicated by the uncertain detection of O III] itself, and by the non detection of C IV. For instance, assuming that O III] was detected, we could obtain [C/O] from the ratio (C IV+C III])/O III] (Pérez-Montero & Amorín 2017). However, different assumptions on the nature of the C IV non detection

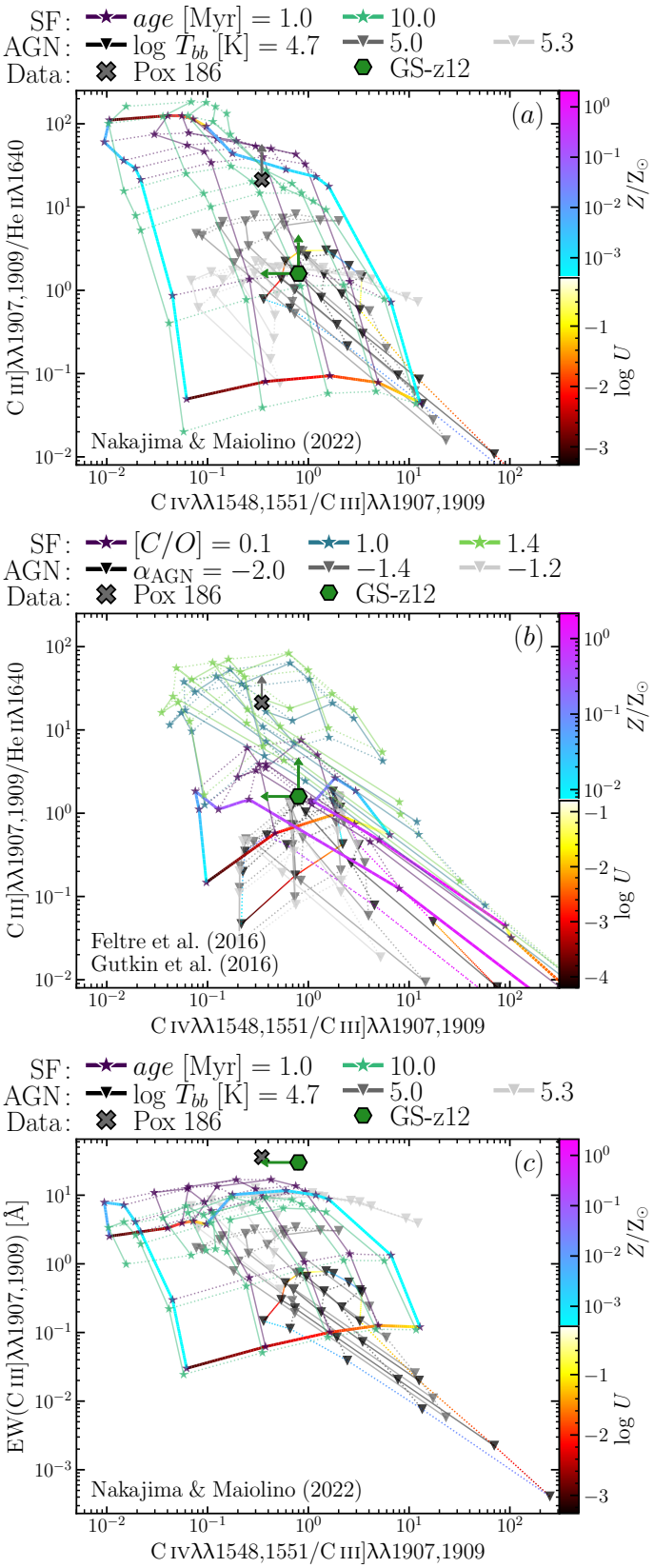

Fig. 4. Photoionisation diagnostic diagrams for GS-z12. Panels a–b; photoionisation diagnostics for star-formation (stars) and AGN (triangles), compared to GS-z12 (hexagon) and to the local analogue Pox 186 (cross, Kumari et al. 2024). Panel c; photoionisation diagnostic with EW(C III]). The grids are from NM22 (panels a and c), and from G16 and F16 (panel b). All upper and lower limits are given at 3 σ.

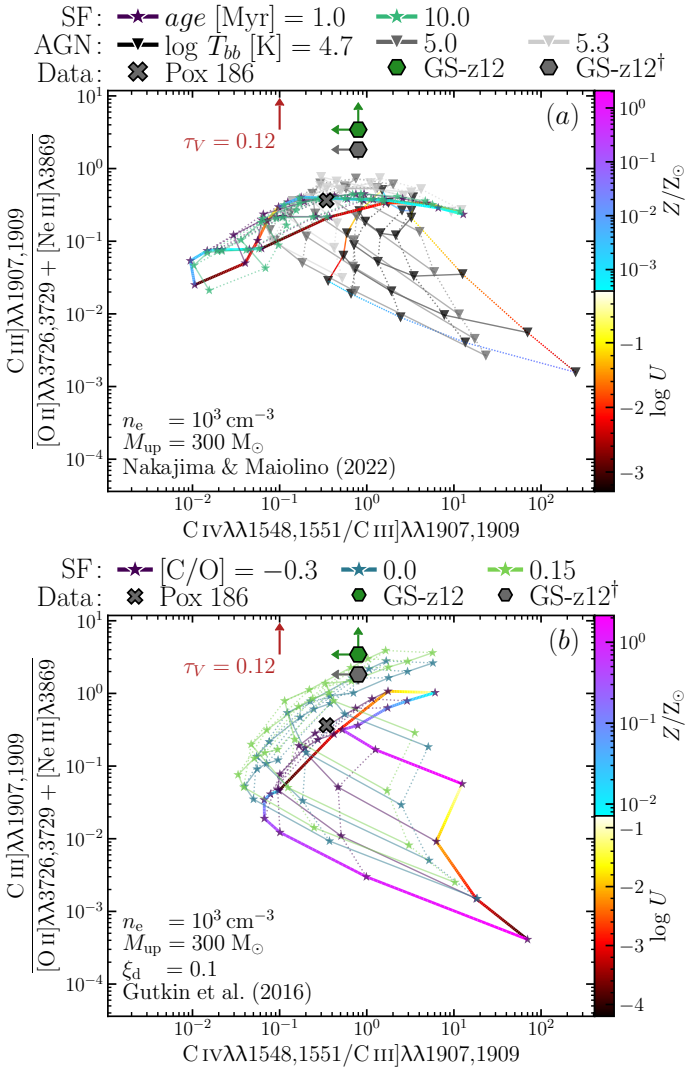

Fig. 5. Abundance diagnostic diagrams. Panel a; our upper limits on GS-z12 (hexagon), compared to photoionisation models powered by star formation (SF; stars) and AGN (triangles; NM22), illustrating that GS-z12 lies well outside the range of grids with solar and subsolar C/O (used by NM22). Panel b; star-forming models of G16, with varying C/O abundance between 0.5 and 1.4 solar. Combining the detection of C III]λ1909 with stringent upper limits on [O II]λλ3726,3729 and [Ne III]λ3869, the models constrain the abundance to super-solar values, i.e. much higher values than what is observed in galaxies at $z = 9$ (see Fig. 6) and in the local analogue Pox 186 (Kumari et al. 2024). Alternatively, assuming both [O II] and [Ne III] to be detected, we obtain the grey hexagon marked with a †, which points to a solar [C/O] – still high for high-redshift galaxies. The red upward arrow marks the magnitude of the dust reddening correction, which we conservatively *do not apply*. We colour code only the external lines in the grids, and only for one of the SF and AGN grids; note the different range of the grid parameters.

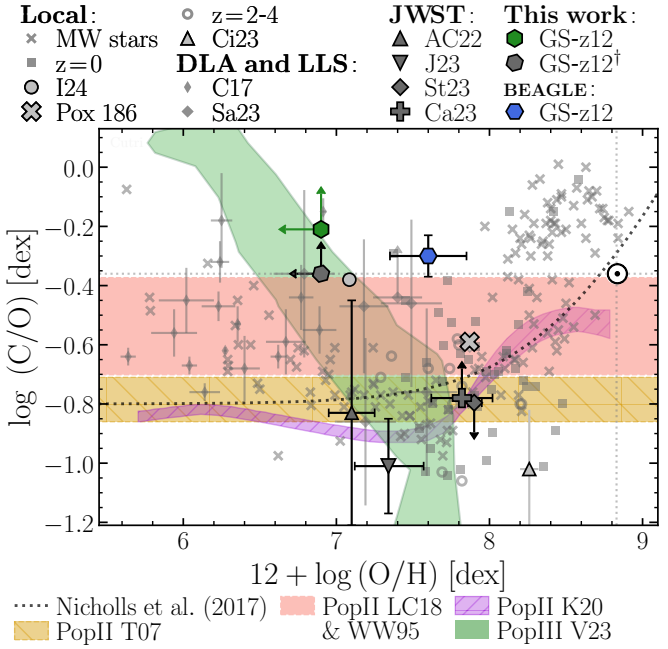

Fig. 6. Compilation of chemical abundance patterns from both local stars and galaxies (see text for references) and from metal-poor galaxies at $z = 2$–9, compared to the yields of PopII and PopIII supernovae. The grey dotted lines are the solar abundances (G16). Regardless of the precise assumptions used, GS-z12 (hexagons) stands out as a metal-poor system with high C/O abundance, and is therefore closer to DLA systems (Cooke et al. 2017, C17; Saccardi et al. 2023, Sa23) than to other high-redshift galaxies recently observed by JWST (Arellano-Córdova et al. 2022, AC22; Jones et al. 2023, J23; Cameron et al. 2023b, Ca23; Stiavelli et al. 2023, St23). The dotted line is the chemical enrichment pattern from Nicholls et al. (2017); the golden horizontal hatched band is the yield of PopII supernovae from Tominaga et al. (2007). The purple region is the PopII abundance pattern from Kobayashi et al. (2020). The red horizontal band is the combined yield of metal-poor Type II supernovae from Woosley & Weaver (1995) and Limongi & Chieffi (2018). The green region is the yield of PopIII supernovae (Heger & Woosley 2010, adapted from Vanni et al. 2023). We adopt the solar abundance ratio log(C/O) = −0.36 (G16).

would give opposite constraints on [C/O], which – for the case of GS-z12 – mean that this estimator is not particularly constraining. In fact, assuming that C IV was dominated by ISM absorption, its non detection could still be consistent with considerable emission-line flux; in this case, we would obtain a lower limit [C/O] > −0.5 dex. In contrast, assuming that the non detection of C IV was due to noise, we obtain a 3-σ upper limit [C/O] < −0.35 dex, in tension with the results from [O II] and [Ne III]. Overall, we deem the results from [O II] and [Ne III] more credible, both because these lines have higher S/N, as well as because they give consistent results, whether they are not detected, or detected but close to the noise level.

Fig. 6 shows the abundance ratio C/O vs. 12 + log (O/H), including Milky Way stars (grey crosses; Gustafsson et al. 1999; Akerman et al. 2004; Fabbian et al. 2009; Nissen et al. 2014), galaxies ranging from the local Universe (squares, labelled $z = 0$; Berg et al. 2016, 2019; Peña-Guerrero et al. 2017; Senchyna et al. 2017) up to Cosmic Noon (empty circles, labelled $z = 2$–4; Erb et al. 2010; Christensen et al. 2012; Bayliss et al. 2014; James et al. 2014; Stark et al. 2014; Berg et al. 2018; Mainali et al. 2020; Matthee et al. 2021; Iani et al. 2023; Citro et al. 2024, labelled Ci23), local dwarf galaxies (Izotov et al. 2024, I24; Kumari et al. 2024, Pox 186), and DLAs (Cooke et al. 2017, C17; Saccardi et al. 2023, Sa23). We also show the abundances (and upper limits) from four high-redshift galaxies at $z = 6$–9 measured by JWST (Arellano-Córdova et al. 2022, AC22; Jones et al. 2023, J23; Cameron et al. 2023b, Ca23; and Stiavelli et al. 2023, St23). These galaxies tend to display a low [C/O] ≈ −0.6 dex, very close to or even lower than the yield of metal-poor Type II supernovae (golden horizontal band, Tominaga et al. 2007; red horizontal band, Woosley & Weaver 1995 and Limongi & Chieffi 2018;

purple region, Kobayashi et al. 2020). Indeed, these galaxies follow qualitatively the enrichment sequence from Nicholls et al. (2017), which is interpreted as a mixing sequence between the pure Type II yields of young, low-metallicity systems, and the later contribution of stars on the asymptotic giant branch (AGB), which have longer enrichment timescales than Type II supernovae (e.g. Salaris et al. 2014).

GS-z12, instead, appears as an outlier relative to other galaxies, but it is consistent with some high-z DLAs. Specifically, the DLA has an upper-limit metallicity of $12 + \log(\mathrm{O/H}) = 6.9$ dex (as estimated from combining N_{HI} and τ_{V}; Sects. 3 and 4), or a value of 7.59 ± 0.25 dex (from BEAGLE; Table 2). The C/O abundance is either a lower limit (based on comparing the C III]/([O II]+[Ne III]) line ratio to models; Sect. 5) or a slightly super-solar value of $[\mathrm{C/O}] = 0.06 \pm 0.07$ (from BEAGLE; Table 2). These abundance values place GS-z12 clearly outside the enrichment sequence of local and lower redshift galaxies, and closer to the decreasing branch occupied by DLAs and extremely metal-poor stars in the Milky Way halo.

When compared with the models discussed above, the chemical enrichment pattern of GS-z12 is inconsistent with pure Type II supernovae yields. Yet, its C/O and low metallicity suggest an enrichment history more similar to DLAs (small grey triangles). The yields of PopIII supernovae from Vanni et al. (2023, green band) give a sequence of super-solar C/O that may explain the lower limit of GS-z12. Crucially, these models produce super-solar C/O via low-energy PopIII supernovae ($E < 2 \times 10^{51}$ erg; Vanni et al. 2023).

6. Summary, discussion, and outlook

JWST NIRSpec MSA observations from the combined programmes PID 1210 and 3215 enabled us to investigate the detailed physical properties of GS-z12, a galaxy at $z > 12$, near Cosmic Dawn. We report the detection of C III] at $z = 12.48$. This is the most distant nebular-line detection to date, and the most distant evidence of chemical enrichment.

A full spectral modelling with the BEAGLE tool confirms the earlier results from CLC23; GS-z12 has a stellar mass $M_\star \sim 5 \times 10^7\,\mathrm{M}_\odot$ and a mass-doubling time of 20 Myr. The fit indicates a moderate dust attenuation optical depth, $\tau_{\mathrm{V}} = 0.20$, and a sub-solar metallicity of $12 + \log(\mathrm{O/H}) = 7.59$ dex, mostly constrained by the weak emission lines.

The redshift obtained through the C III] line implies that the Lyα drop has a prominent damping wing. This cannot be associated only with IGM absorption, but can be modelled with absorption by the ISM of the galaxy or its CGM (i.e. a local DLA). Specifically, thanks to the accurate redshift obtained from the nebular emission lines, we can reliably model the damping wing profile and infer a high column density of $N_{\mathrm{HI}} \approx 10^{22}\,\mathrm{cm}^{-2}$. The inferred gas fraction ($M_{\mathrm{gas}}/M_\star$) is about 0.5, consistent with what one would expect at these high redshifts (Carilli & Walter 2013; Tacconi et al. 2020). We note, however, that the uncertainties on the conversion from N_{HI} to M_{gas} and on the stellar mass-to-light ratio (due for instance to a top-heavy IMF, e.g. Rusakov et al. 2023) can be large. Converting this gas mass and the BEAGLE SFR into surface densities, we obtain values of $150\,\mathrm{M}_\odot\,\mathrm{pc}^{-2}$ and $25\,\mathrm{M}_\odot\,\mathrm{yr}^{-1}\,\mathrm{kpc}^{-2}$, respectively. This combination is higher than the predictions from the local S–K relation (Kennicutt & Evans 2012), suggesting that we are missing a substantial fraction of the gas, very likely in molecular form, or that our SFRs are significantly overestimated.

The gas metallicity we infer from N_{HI} is also quite uncertain, given the unwarranted assumption that τ_{V} estimated from the stellar continuum also applies to the Lyα absorber. This is compounded by the large uncertainties on the dust-to-metal ratio (ξ_{d}) at these early epochs. With an average estimate of $\xi_{\mathrm{d}} = 0.24$ (Konstantopoulou et al. 2022) we obtain a sub-solar metallicity of about 0.005–0.02 solar, smaller than the value inferred from BEAGLE.

The high EW(C III]) is reminiscent of lower-redshift AGN (Le Fèvre et al. 2019), but the lack of C IV emission seems at odds with this scenario. Unfortunately, and in spite of a 50 h-long integration, the upper limits on C IV and He II are unable to definitely rule out the presence of an AGN (Figs. 4a–b; we set a threshold of 3-σ for the non detections, or 99.9% confidence). A local galaxy with properties analogue to GS-z12, i.e. with a high-EW C III] emission, is the low-mass, metal-poor star-forming dwarf galaxy Pox 186 (Kumari et al. 2024). GS-z12 and Pox 186 have similar size of ≈100 pc, yet, they have different masses (by two orders of magnitude) and markedly different C/O abundances.

The detection of C III], and its high EW, rules out scenarios of pristine stellar populations (PopIII) or black holes (direct-collapse black holes; NM22). The high-EW value of 30 ± 7 Å cannot be explained with the sub-solar C/O ratio of the NM22 models. Kumari et al. (2024) have found similar difficulties in explaining the emission-line properties of Pox 186 (grey cross in Fig. 4c) – perhaps exacerbated by the sub-solar C/O measured in their dwarf galaxy.

The long integration time of these observations provides stringent upper limits on both [O II] and [Ne III], which we use to study the C/O ratio (Fig. 5). The inability of models with sub-solar C/O to explain the observed lower limits on C III]/([O II]+[Ne III]) suggests that the bulk of the gas in GS-z12 has solar to super-solar C/O abundance. While the prism data indicate a tentative detection of [O II] and [Ne III], we do not consider these detections to be robust (see Sect. 2.3). Nevertheless, if we replace the 3-σ upper limits in C III]/([O II]+[Ne III]) with detections, the line ratio decreases from 3.4 down to 1.8, which would still require a solar C/O (Fig. 5). In addition, throughout our analysis we do not apply any dust correction, but we note that any correction would increase the C III]/([O II]+[Ne III]) ratio and the C/O abundance, making our result even stronger. Indeed, self-consistent Bayesian modelling with BEAGLE confirms these results, requiring an abundance ratio $[\mathrm{C/O}] = 0.06 \pm 0.07$ (Table 2 and Fig. 2).

We note that the lower limit on C/O that we obtain is based on models, which rely on several assumptions about the shape of the ionising sources and the gas chemical abundance patterns. However, we also tune the model parameters to take into account some of the possible systematic differences between $z = 12$ and lower-redshift galaxies, using a higher upper-mass cutoff of the IMF and marginalising over $\log(\mathrm{U})$ and ξ_{d}. With this approach, we find valuable implications on the chemical evolution history of this early galaxy.

In Fig. 6, we showed the location of GS-z12 in the O/H vs. C/O enrichment diagram. Regardless of the method adopted, the high C/O and low metallicity of this galaxy are inconsistent with the yields of Type II supernovae ($[\mathrm{C/O}] \lesssim -0.15$ dex), and much higher than what found by JWST in galaxies at $z = 6$–9 (Arellano-Córdova et al. 2022; Jones et al. 2023; Cameron et al. 2023b; Stiavelli et al. 2023).

Stars with extremely high C abundance have been found in the Milky Way, and these have some of the lowest measured Fe/H abundances (Aoki et al. 2006). While for these old galactic stars other enrichment channels are possible (dredge up or interactions with AGB companions), these scenarios seem inad-

equate for the case of GS-z12, as dredge up is most appropriate for evolved low-mass stars (as is the case for Aoki et al. 2006). Specifically, AGB stars would need to dominate the chemical enrichment history of GS-z12, but at $z = 12.48$ only stars more massive than $3\,M_\odot$ have had sufficient time to reach this phase, implying that the chemical enrichment history is still dominated by core-collapse supernovae. Moreover, most metal-poor, C-rich stars in the Milky Way have solar or even sub-solar C/O abundance (with the results of Aoki et al. 2006 representing the exception, having [C/O] > 0.26).

A possible explanation for this anomalously high [C/O] value is that the stars in GS-z12 carry the signature of chemical enrichment due to massive, metal-poor stars, whose yields can be significantly different than those of PopII Type II supernovae. In particular, chemical enrichment from PopIII can potentially explain the observed C/O in GS-z12 (Heger & Woosley 2010; Limongi & Chieffi 2018), especially when including low-energy supernova explosions (Vanni et al. 2023). These explosions leave remnants with a higher fraction of the O-rich shell locked in them, with respect to the C-rich shell, thereby increasing the C/O yield of the ejecta to solar or even super-solar values. An early C enrichment channel could be supported by the findings in low-metallicity DLAs and LLS (e.g. Cooke et al. 2017; Saccardi et al. 2023), and by the recent finding of carbonaceous dust in a galaxy at $z = 7$ (Witstok et al. 2023). An alternative explanation is represented by peculiar SFHs, such as those invoked to explain the abundance patterns in GN-z11 (Kobayashi & Ferrara 2024). Such peculiar SFHs would, however, also produce a strong nitrogen abundance, which is inconsistent with the observations of GS-z12.

It remains to be seen whether such high C/O abundances can be explained by galaxy-scale chemical enrichment histories. Yields with super-solar C/O are predicted for PopIII stars with initial mass below 10–20 $M_\odot$ (Heger & Woosley 2010; Limongi & Chieffi 2012). More massive PopIII stars (40–60 $M_\odot$) may also have super-solar C/O yields, if their supernova explosions have low energy (Heger & Woosley 2010). Crucially, when metallicity increases, the C/O of supernovae yields decreases, converging to the sub-solar values of PopII stars. The BEAGLE metallicity is up to a dex higher compared to low-mass DLAs (Welsh et al. 2019, although our metallicity uncertainties are large). This relatively high metallicity would likely require multiple generations of stars, in tension with an enrichment scenario driven by Pop-III stars. The metallicity constraints from the DLA are much lower, but these are also very uncertain, due to a number of underlying assumptions that we cannot constrain from the data. In summary, uncertainties on the absolute metallicity determination prevent us from drawing strong conclusions on the chemical enrichment history of this galaxy, yet the high [C/O] ratio makes GS-z12 unique compared to other high-redshift sources discovered by JWST.

This detection of the most distant metal transition, which has provided such precious information about the earliest phases of the chemical enrichment, has required a very long exposure (65 h, although mostly as a parallel observation). This is due to the extreme faintness of such distant galaxies. However, in the future, large-area surveys and gravitational lenses may help identify more high-redshift galaxies that are sufficiently bright for deep spectroscopic follow-up with shorter exposures.

Acknowledgements. We are grateful to S. Salvadori and I. Vanni for providing the chemical enrichment tracks for some Population III scenarios. We thank N. Laporte and V. Iršič for useful discussions and suggestions. FDE, RM, JW, WB, TJL acknowledge support by the Science and Technology Facilities Council (STFC), by the ERC through Advanced Grant 695671 "QUENCH", and by the UKRI Frontier Research grant RISEandFALL. RM also acknowledges funding from a research professorship from the Royal Society. SC and GV acknowledge support by European Union's HE ERC Starting Grant No. 101040227 - WINGS. ECL acknowledges support of an STFC Webb Fellowship (ST/W001438/1). AJB and JC acknowledge funding from the "FirstGalaxies" Advanced Grant from the European Research Council (ERC) under the European Union's Horizon 2020 research and innovation programme (Grant agreement No. 789056). SA acknowledges support from Grant PID2021-127718NB-I00 funded by the Spanish Ministry of Science and Innovation/State Agency of Research (MICIN/AEI/10.13039/501100011033). This research is supported in part by the Australian Research Council Centre of Excellence for All Sky Astrophysics in 3 Dimensions (ASTRO 3D), through project number CE170100013. KH, ZJ, BDJ, MR, BR and CNAW acknowledge support from the JWST/NIRCam Science Team contract to the University of Arizona, NAS5-02015; DJE is also supported as a Simons Investigator. KN acknowledges support from JSPS KAKENHI Grant JP20K22373. RS acknowledges support from a STFC Ernest Rutherford Fellowship (ST/S004831/1). HÜ gratefully acknowledges support by the Isaac Newton Trust and by the Kavli Foundation through a Newton-Kavli Junior Fellowship. This work was performed using resources provided by the Cambridge Service for Data Driven Discovery (CSD3) operated by the University of Cambridge Research Computing Service (www.csd3.cam.ac.uk), provided by Dell EMC and Intel using Tier-2 funding from the Engineering and Physical Sciences Research Council (capital grant EP/T022159/1), and DiRAC funding from the Science and Technology Facilities Council (www.dirac.ac.uk). This work also made extensive use of the freely available Debian GNU/Linux operative system. We used the Python programming language (van Rossum 1995), maintained and distributed by the Python Software Foundation. We further acknowledge direct use of astropy (Astropy Collaboration 2013), BEAGLE (Chevallard & Charlot 2016), matplotlib (Hunter 2007), numpy (Harris et al. 2020), scikit-learn (Pedregosa et al. 2011), scipy (Virtanen et al. 2020) and topcat (Taylor 2005).

References

Akerman, C. J., Carigi, L., Nissen, P. E., Pettini, M., & Asplund, M. 2004, A&A, 414, 931
Aoki, W., Frebel, A., Christlieb, N., et al. 2006, ApJ, 639, 897
Arellano-Córdova, K. Z., Esteban, C., García-Rojas, J., & Méndez-Delgado, J. E. 2021, MNRAS, 502, 225
Arellano-Córdova, K. Z., Berg, D. A., Chisholm, J., et al. 2022, ApJ, 940, L23
Arrabal Haro, P., Dickinson, M., Finkelstein, S. L., et al. 2023, ApJ, 951, L22
Asplund, M., Grevesse, N., Sauval, A. J., & Scott, P. 2009, ARA&A, 47, 481
Astropy Collaboration (Robitaille, T. P., et al.) 2013, A&A, 558, A33
Baker, W. M., Tacchella, S., Johnson, B. D., et al. 2023, Nat. Astron., submitted [arXiv:2306.02472]
Bayliss, M. B., Rigby, J. R., Sharon, K., et al. 2014, ApJ, 790, 144
Berg, D. A., Skillman, E. D., Henry, R. B. C., Erb, D. K., & Carigi, L. 2016, ApJ, 827, 126
Berg, D. A., Erb, D. K., Auger, M. W., Pettini, M., & Brammer, G. B. 2018, ApJ, 859, 164
Berg, D. A., Erb, D. K., Henry, R. B. C., Skillman, E. D., & McQuinn, K. B. W. 2019, ApJ, 874, 93
Bunker, A. J., Saxena, A., Cameron, A. J., et al. 2023a, A&A, 677, A88
Bunker, A. J., Cameron, A. J., Curtis-Lake, E., et al. 2023b, A&A, submitted [arXiv:2306.02467]
Cameron, A. J., Saxena, A., Bunker, A. J., et al. 2023a, A&A, 677, A115
Cameron, A. J., Katz, H., Rey, M. P., & Saxena, A. 2023b, MNRAS, 523, 3516
Cappellari, M., Scott, N., Alatalo, K., et al. 2013, MNRAS, 432, 1709
Carilli, C. L., & Walter, F. 2013, ARA&A, 51, 105
Carniani, S., Venturi, G., Parlanti, E., et al. 2024, A&A, 685, A99
Chabrier, G. 2003, PASP, 115, 763
Charbonnel, C., Schaerer, D., Prantzos, N., et al. 2023, A&A, 673, L7
Charlot, S., & Fall, S. M. 2000, ApJ, 539, 718
Chevallard, J., & Charlot, S. 2016, MNRAS, 462, 1415
Christensen, L., Laursen, P., Richard, J., et al. 2012, MNRAS, 427, 1973
Citro, A., Berg, D. A., Erb, D. K., et al. 2024, ApJ, 969, 21
Cooke, R. J., Pettini, M., & Steidel, C. C. 2017, MNRAS, 467, 802
Curti, M., D'Eugenio, F., Carniani, S., et al. 2023, MNRAS, 518, 425
Curti, M., Maiolino, R., Curtis-Lake, E., et al. 2024, A&A, 684, A75
Curtis-Lake, E., Carniani, S., Cameron, A., et al. 2023, Nat. Astron., 7, 622
De Cia, A., Ledoux, C., Mattsson, L., et al. 2016, A&A, 596, A97
de Graaff, A., Rix, H.-W., Carniani, S., et al. 2024, A&A, 684, A87
De Vis, P., Jones, A., Viaene, S., et al. 2019, A&A, 623, A5
Dopita, M. A., Fischera, J., Sutherland, R. S., et al. 2006, ApJS, 167, 177
Dorner, B. 2012, Theses, Université Claude Bernard, Lyon I, France
Dorner, B., Giardino, G., Ferruit, P., et al. 2016, A&A, 592, A113
Dressler, A., Rieke, M., Eisenstein, D., et al. 2024, ApJ, 964, 150

Eisenstein, D. J., Willott, C., Alberts, S., et al. 2023a, ApJS, submitted [arXiv:2306.02465]
Eisenstein, D. J., Johnson, B. D., Robertson, B., et al. 2023b, ApJS, submitted [arXiv:2310.12340]
Endsley, R., Stark, D. P., Whitler, L., et al. 2023, MNRAS, submitted [arXiv:2306.05295]
Erb, D. K., Pettini, M., Shapley, A. E., et al. 2010, ApJ, 719, 1168
Fabbian, D., Nissen, P. E., Asplund, M., Pettini, M., & Akerman, C. 2009, A&A, 500, 1143
Feltre, A., Charlot, S., & Gutkin, J. 2016, MNRAS, 456, 3354
Ferruit, P., Jakobsen, P., Giardino, G., et al. 2022, A&A, 661, A81
Foreman-Mackey, D., Hogg, D. W., Lang, D., & Goodman, J. 2013, PASP, 125, 306
Frebel, A., & Norris, J. E. 2015, ARA&A, 53, 631
Fudamoto, Y., Smit, R., Bowler, R. A. A., et al. 2022, ApJ, 934, 144
Fumagalli, M., O'Meara, J. M., & Prochaska, J. X. 2016, MNRAS, 455, 4100
Gustafsson, B., Karlsson, T., Olsson, E., Edvardsson, B., & Ryde, N. 1999, A&A, 342, 426
Gutkin, J., Charlot, S., & Bruzual, G. 2016, MNRAS, 462, 1757
Harris, C. R., Millman, K. J., van der Walt, S. J., et al. 2020, Nature, 585, 357
Heger, A., & Woosley, S. E. 2010, ApJ, 724, 341
Heintz, K. E., Watson, D., Brammer, G., et al. 2024, Science, 384, 890
Hirano, S., Hosokawa, T., Yoshida, N., et al. 2014, ApJ, 781, 60
Hosokawa, T., Omukai, K., Yoshida, N., & Yorke, H. W. 2011, Science, 334, 1250
Hsiao, T. Y. Y., Abdurro'uf, Coe, D., et al. 2023, ApJ, submitted [arXiv:2305.03042]
Hunter, J. D. 2007, Comput. Sci. Eng., 9, 90
Iani, E., Zanella, A., Vernet, J., et al. 2023, MNRAS, 518, 5018
Izotov, Y. I., Schaerer, D., Guseva, N. G., Thuan, T. X., & Worseck, G. 2024, MNRAS, 528, L10
Jakobsen, P., Ferruit, P., Alves de Oliveira, C., et al. 2022, A&A, 661, A80
James, B. L., Pettini, M., Christensen, L., et al. 2014, MNRAS, 440, 1794
Jones, T., Sanders, R., Chen, Y., et al. 2023, ApJ, 951, L17
Kennicutt, R. C., & Evans, N. J. 2012, ARA&A, 50, 531
Kobayashi, C., & Ferrara, A. 2024, ApJ, 962, L6
Kobayashi, C., Karakas, A. I., & Lugaro, M. 2020, ApJ, 900, 179
Konstantopoulou, C., De Cia, A., Krogager, J.-K., et al. 2022, A&A, 666, A12
Konstantopoulou, C., De Cia, A., Ledoux, C., et al. 2024, A&A, 681, A64
Kumari, N., Smit, R., Leitherer, C., et al. 2024, MNRAS, 529, 781
Kunth, D., Sargent, W. L. W., & Kowal, C. 1981, A&AS, 44, 229
Le Fèvre, O., Lemaux, B. C., Nakajima, K., et al. 2019, A&A, 625, A51
Limongi, M., & Chieffi, A. 2012, ApJS, 199, 38
Limongi, M., & Chieffi, A. 2018, ApJS, 237, 13
Looser, T. J., D'Eugenio, F., Maiolino, R., et al. 2023, arXiv e-prints [arXiv:2306.02470]
Mainali, R., Stark, D. P., Tang, M., et al. 2020, MNRAS, 494, 719
Maiolino, R., Scholtz, J., Witstok, J., et al. 2024, Nature, 627, 59
Matthee, J., Sobral, D., Hayes, M., et al. 2021, MNRAS, 505, 1382
Nakajima, K., & Maiolino, R. 2022, MNRAS, 513, 5134
Nakajima, K., Ouchi, M., Isobe, Y., et al. 2023, ApJS, 269, 33
Nicholls, D. C., Sutherland, R. S., Dopita, M. A., Kewley, L. J., & Groves, B. A. 2017, MNRAS, 466, 4403
Nissen, P. E., Chen, Y. Q., Carigi, L., Schuster, W. J., & Zhao, G. 2014, A&A, 568, A25
Oesch, P. A., Brammer, G., van Dokkum, P. G., et al. 2016, ApJ, 819, 129
Peña-Guerrero, M. A., Leitherer, C., de Mink, S., Wofford, A., & Kewley, L. 2017, ApJ, 847, 107
Pedregosa, F., Varoquaux, G., Gramfort, A., et al. 2011, J. Mach. Learn. Res., 12, 2825
Pérez-Montero, E., & Amorín, R. 2017, MNRAS, 467, 1287
Pettini, M., Zych, B. J., Steidel, C. C., & Chaffee, F. H. 2008, MNRAS, 385, 2011
Planck Collaboration VI. 2020, A&A, 641, A6
Rawle, T. D., Giardino, G., Franz, D. E., et al. 2022, SPIE Conf. Ser., 12180, 121803R
Reddy, N. A., Topping, M. W., Sanders, R. L., Shapley, A. E., & Brammer, G. 2023, ApJ, 952, 167
Rieke, M. J., Robertson, B., Tacchella, S., et al. 2023, ApJS, 269, 16
Robertson, B. E. 2022, ARA&A, 60, 121
Robertson, B. E., Tacchella, S., Johnson, B. D., et al. 2023, Nat. Astron., 7, 611
Rusakov, V., Steinhardt, C. L., & Sneppen, A. 2023, ApJS, 268, 10
Saccardi, A., Salvadori, S., D'Odorico, V., et al. 2023, ApJ, 948, 35
Salaris, M., Weiss, A., Cassarà, L. P., Piovan, L., & Chiosi, C. 2014, A&A, 565, A9
Salvadori, S., & Ferrara, A. 2012, MNRAS, 421, L29
Schaerer, D., Marques-Chaves, R., Barrufet, L., et al. 2022, A&A, 665, L4
Senchyna, P., Stark, D. P., Vidal-García, A., et al. 2017, MNRAS, 472, 2608
Senchyna, P., Plat, A., Stark, D. P., et al. 2024, ApJ, 966, 92
Stark, D. P., Richard, J., Siana, B., et al. 2014, MNRAS, 445, 3200
Stark, D. P., Ellis, R. S., Charlot, S., et al. 2017, MNRAS, 464, 469
Stiavelli, M., Morishita, T., Chiaberge, M., et al. 2023, ApJ, 957, L18
Tacchella, S., Eisenstein, D. J., Hainline, K., et al. 2023, ApJ, 952, 74
Tacconi, L. J., Genzel, R., & Sternberg, A. 2020, ARA&A, 58, 157
Taylor, M. B. 2005, ASP Conf. Ser., 347, 29
Tominaga, N., Umeda, H., & Nomoto, K. 2007, ApJ, 660, 516
Vanni, I., Salvadori, S., Skúladóttir, Á., Rossi, M., & Koutsouridou, I. 2023, MNRAS, 526, 2620
van Rossum, G. 1995, CWI Technical Report, CS-R9526
Virtanen, P., Gommers, R., Oliphant, T. E., et al. 2020, Nature Methods, 17, 261
Wang, B., Fujimoto, S., Labbé, I., et al. 2023, ApJ, 957, L34
Welsh, L., Cooke, R., & Fumagalli, M. 2019, MNRAS, 487, 3363
Witstok, J., Shivaei, I., Smit, R., et al. 2023, Nature, 621, 267
Witstok, J., Smit, R., Saxena, A., et al. 2024, A&A, 682, A40
Woosley, S. E., & Weaver, T. A. 1995, ApJS, 101, 181
Zhu, H., Tian, W., Li, A., & Zhang, M. 2017, MNRAS, 471, 3494

[1] Kavli Institute for Cosmology, University of Cambridge, Madingley Road, Cambridge CB3 0HA, UK
[2] Cavendish Laboratory, University of Cambridge, 19 JJ Thomson Avenue, Cambridge CB3 0HE, UK
[3] Department of Physics and Astronomy, University College London, Gower Street, London WC1E 6BT, UK
[4] Scuola Normale Superiore, Piazza dei Cavalieri 7, I-56126 Pisa, Italy
[5] Department of Physics, University of Oxford, Denys Wilkinson Building, Keble Road, Oxford OX1 3RH, UK
[6] Centre for Astrophysics Research, Department of Physics, Astronomy and Mathematics, University of Hertfordshire, Hatfield AL10 9AB, UK
[7] Sorbonne Université, CNRS, UMR 7095, Institut d'Astrophysique de Paris, 98 bis bd Arago, 75014 Paris, France
[8] Centro de Astrobiología (CAB), CSIC-INTA, Cra. de Ajalvir Km. 4, 28850 Torrejón de Ardoz, Madrid, Spain
[9] School of Physics, University of Melbourne, Parkville 3010, VIC, Australia
[10] ARC Centre of Excellence for All Sky Astrophysics in 3 Dimensions (ASTRO 3D), Australia
[11] European Southern Observatory, Karl-Schwarzschild-Strasse 2, 85748 Garching, Germany
[12] Center for Astrophysics | Harvard & Smithsonian, 60 Garden St., Cambridge, MA 02138, USA
[13] Steward Observatory, University of Arizona, 933 North Cherry Avenue, Tucson, AZ 85721, USA
[14] AURA for European Space Agency, Space Telescope Science Institute, 3700 San Martin Drive, Baltimore, MD 21210, USA
[15] National Astronomical Observatory of Japan, 2-21-1 Osawa, Mitaka, Tokyo 181-8588, Japan
[16] Department for Astrophysical and Planetary Science, University of Colorado, Boulder, CO 80309, USA
[17] Department of Astronomy and Astrophysics, University of California, Santa Cruz, 1156 High Street, Santa Cruz, CA 95064, USA
[18] Astrophysics Research Institute, Liverpool John Moores University, 146 Brownlow Hill, Liverpool L3 5RF, UK
[19] NRC Herzberg, 5071 West Saanich Rd, Victoria, BC V9E 2E7, Canada

Appendix A: In-depth analysis of the data

In Sects. 2.2 and 2.3 we summarised our considerations on the reliability of the emission lines detections. The goal of this section is to provide more information on the data and on the reliability of the various emission-line detections – particularly in the low-S/N regime. To do so, we take advantage of 162 individual integrations for GS-z12, each with 1,400.5 s duration. We show the S/N as a function of wavelength for each of these detections in Fig. A.1a; the y-axis values from 0 to 113 correspond to the 114 integrations five visits from PID 3215; the remaining 48 integrations are from two visits in PID 1210. We saturate the colour limits between S/N 0 and 2, to highlight a faint vertical line at 2.57 μm, which we interpret as C III]. No other emission lines are clearly visible in this representation. In particular, we see no evidence for [O II] or [Ne III]; even though these two lines have lower S/N than C III] (which should make them harder too see), they occupy a region of the spectrum with lower continuum flux than C III] (which would enhance the contrast with neighbouring pixels). The 162 individual spectra are also shown in panel b; while this figure is dominated by noise, the C III] line is also visible here. Panel c shows the 16th, 50th, and 84th percentiles of the data in panel b. The vertical lines mark the locations of O III], C III], [O II], and [Ne III]. In this figure, C III] and [O II] are clearly seen, while O III] seems absent and so does [Ne III]. This line in particular has an ugly spectral profile, which further validates our decision to treat it as a tentative detection only.

Panel d shows a comparison between the noise of our co-added data, derived from the data reduction pipeline (black) and the dispersion of the 162 exposures (grey), estimated as the 84th-16th inter-percentile range divided by $2 \cdot \sqrt{162}$. The latter estimate is 25–30 per cent smaller than the former, but it does not take into account correlated noise due to spectral resampling on the NIRSpec detector. In contrast, the data reduction pipeline implements an effective correction to the noise (Dorner et al. 2016), giving a more conservative estimate. Using the grey curve as noise vector, the C III] S/N would increase to 7–7.5.

Finally, in panel e we show the 1-d spectra from PID 1210 (cyan) and 3215 (sand), including zoom-in windows around the Lyα drop, O III]–C III] and [O II]-[Ne III] (panels f–h). This comparison in particular shows that O III] seems absent in 3215, but a single high pixel in 1210 may be driving its 2.3 tentative detection; C III], in contrast, appears to have similar profiles at the same location in both 1210 and 3215 (panel g). [O II] appears both in 1210 and 3215, but, as we have mentioned, its wavelength is different between the two observations. An issue due to the wavelength solution seems unlikely, because the galaxy is well centred in the MSA shutter, and because the shift in spectral pixels due to intra-shutter position is negligible at these red wavelengths. If any problem in the wavelength calibration was present, it could potentially explain the moderate mismatch in redshift between C III] and [O II]–[Ne III]. [Ne III] confirms its dubious nature, especially in 1210, where it shows a narrow profile that does not resemble a true emission line.

In Fig. A.2 we show the jackknife spectra obtained by stacking all the individual integrations, but excluding the integrations from a single visit at a time. This procedure highlights whether the emission lines we see in the data arise from a detector feature, which may be in common between all the integrations from the same visit.

The stacked spectra are obtained by applying an iterative 3-σ clipping algorithm in each wavelength pixel, and by applying inverse- variance weighting. We fit a single Gaussian with a local linear background around each of O III], C III], [O II], and [Ne III]. Overall, we find that C III] is confirmed at 5-σ significance, and does not appear to be driven by any single visit. The uncertainties about O III] and [Ne III] are larger than in the fiducial fit, reflecting the increased number of free parameters used here.

We perform the same test in the left column of Fig A.3, but only for PID 3215, because in PID 1210 the G395M exposure time is much shorter than in PID 3215 (only 10 per cent of the total time, Table 1). We find no evidence of strong artefacts in any of the visits. As a recovery test, we add a single Gaussian emission line with flux equal to the [O II] flux measured from the prism, dispersion equal to one pixel, and centred at the expected location of the [O II] doublet (vertical dashed lines). The second and third columns in Fig A.3 show a comparison between the data without and with the artificial line injection. This is the best-case scenario of a single, spectrally unresolved emission line; any additional broadening (e.g. due to the doublet nature of [O II]) would make the following estimates more conservative. We estimate the line sensitivity by integrating the variance spectrum from the pipeline over two spectral pixels; based on the (conservative) pipeline uncertainties, we should be able to measure this artificial line with S/N=3. This would suggest that at least one of [O II] or [Ne III] should be seen in the grating data. However, the injection test shows that the effective S/N of the artificial line is likely lower than three, and that we would not be able to detect [O II] or [Ne III].

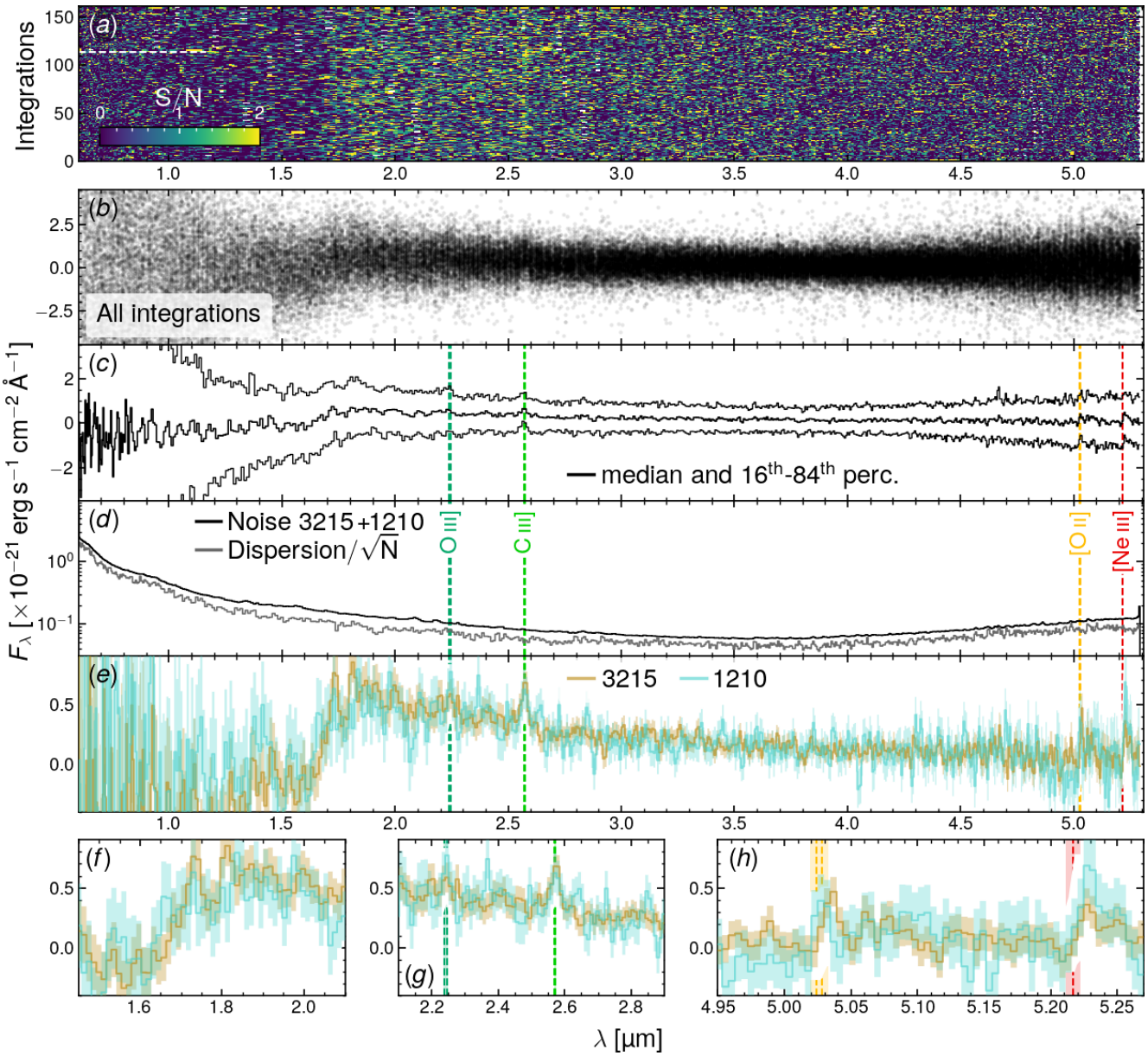

Fig. A.1. Summary of the prism observations. Panel a; S/N of each of the 162 individual integrations. The horizontal dashed line separates the bottom 114 rows with the 3215 integrations from the 1210 integrations above. Panel b; spectrum of each of the individual integrations. A feature at the location of C III] is clearly seen. Panel c; median and 16th–84th percentile of panel b, showing again the presence of C III], and the possible presence of [O II]. Panel d; comparison between the noise estimated by the data reduction pipeline (black) with the noise estimated from the dispersion of the integrations (grey, calculated under a Gaussian-noise assumption). Panels e–h; comparison between 3215 (sand) and 1210 (cyan), showing that C III] is seen in both programmes; in contrast, O III] is not seen in 3215 (the deepest of the two surveys); an emission line close to the position of [O II] is seen in both surveys, but at different wavelengths; [Ne III] is seen in 3215, but has an unconvincing line profile in 1210.

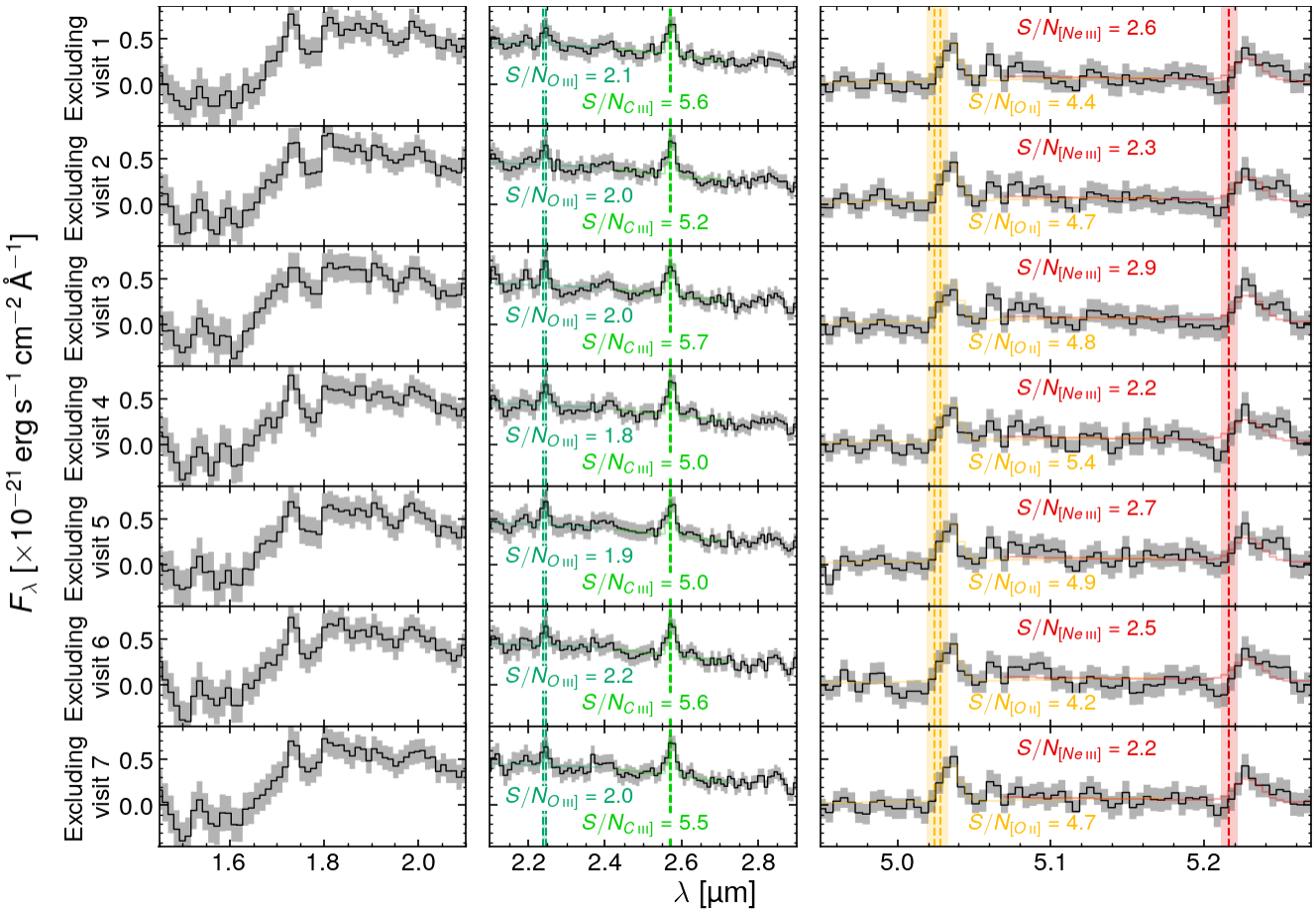

Fig. A.2. Jackknife combination of the prism data; each row is obtained by excluding all the integrations from one of the seven visits and combining the rest. The first two rows exclude the first and second visit from PID 1210; the bottom five rows each exclude one of the visits from PID 3215. The vertical dashed lines and shaded regions are the same as in Figs. 1 and A.1. The labels report the S/N of each line. C III] appears well detected in all combinations, meaning that this line is unlikely to arise from detector artefacts (which may be present in all the integrations from the same visit). The different S/N compared to the fiducial fits are due to the different model adopted here (see text for more details).

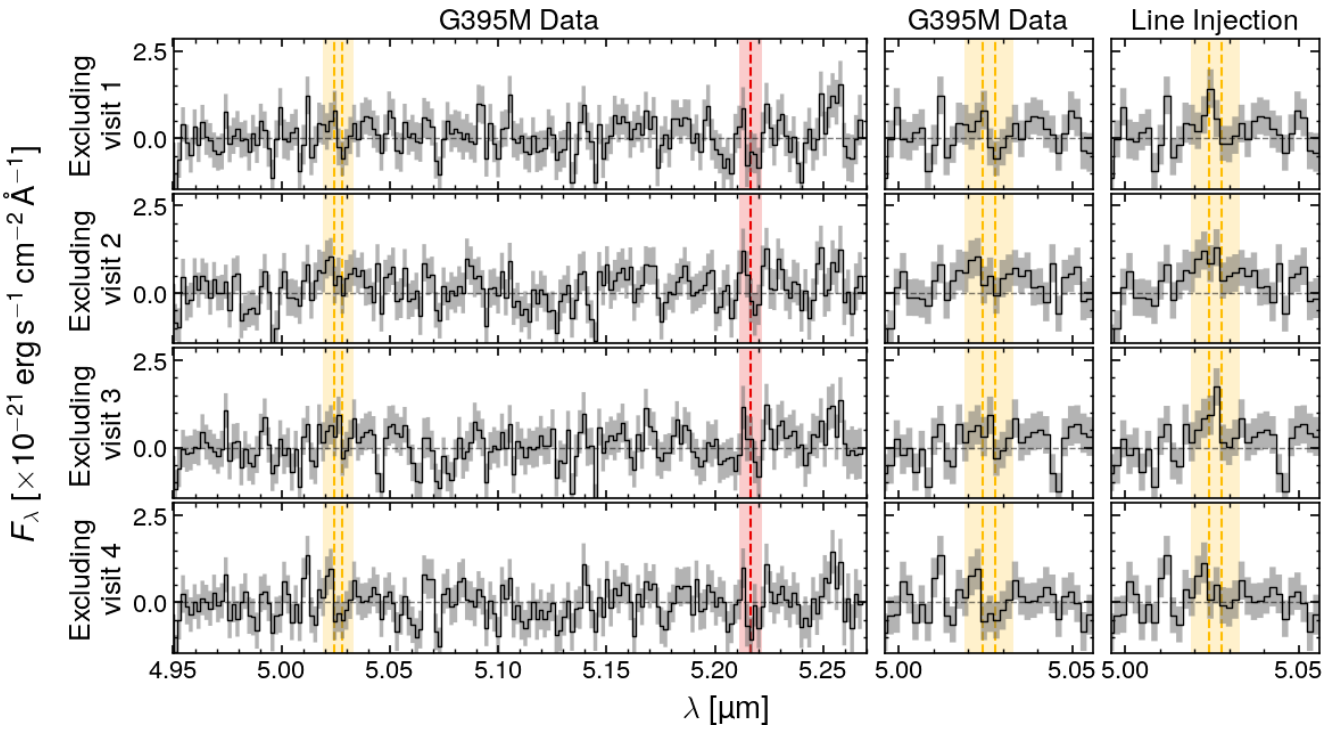

Fig. A.3. Jackknife combination of the G395M grating data; each row is obtained by excluding all the integrations from one of the four visits in PID 3215 and combining the rest (see Table 1). The first column displays the spectral region of interest, the second column is a zoom-in on the region of [O II], the third column is the same as the second, but we added a Gaussian emission line with total flux equal to the [O II] flux measured in the prism. The vertical dashed lines and shaded regions are the same as in Figs. 1 and A.1 and highlight the expected wavelengths of [O II] (orange) and [Ne III] (red). Given the noise of these observations, this line is unlikely to arise from detector artefacts (which may be present in all the integrations from the same visit). The different S/N compared to the fiducial fits are due to the different model adopted here (see text for more details).